

RESEARCH ARTICLE

A fully coupled high-order discontinuous Galerkin method for diffusion flames in a low-Mach number framework

Juan Gutiérrez-Jorquera¹  | Florian Kummer^{1,2}

¹Chair of Fluid Dynamics, Technical University of Darmstadt, Darmstadt, Germany

²Centre for Computational Engineering, Technical University of Darmstadt, Darmstadt, Germany

Correspondence

Florian Kummer, Centre for Computational Engineering, Technical University of Darmstadt, Otto-Berndt-Str. 2, 64287 Darmstadt, Germany.
Email: kummer@fdy.tu-darmstadt.de

Funding information

Deutsche Forschungsgemeinschaft, Grant/Award Number: OB 96/47-1

Abstract

We present a fully coupled solver based on the discontinuous Galerkin method for steady-state diffusion flames using the low-Mach approximation of the governing equations with a one-step kinetic model. The nonlinear equation system is solved with a Newton–Dogleg method and initial estimates for flame calculations are obtained from a flame-sheet model. Details on the spatial discretization and the nonlinear solver are presented. The method is tested with reactive and nonreactive benchmark cases. Convergence studies are presented, and we show that the expected convergence rates are obtained. The solver for the low-Mach equations is used for calculating a differentially heated cavity configuration, which is validated against benchmark solutions. Additionally, a two-dimensional counter diffusion flame is calculated, and the results are compared with the self-similar one dimensional solution of said configuration.

KEYWORDS

diffusion flames, discontinuous Galerkin, high-order methods, low-Mach equations, Newton method

1 | INTRODUCTION AND STATE OF THE ART

High order discretization methods is a topic which has been gaining increasing attention in the last decades. An important exponent of them is the discontinuous Galerkin (DG) method.¹ The DG method was initially developed and utilized for solving hyperbolic conservation laws, especially in the field of computational fluid dynamics (CFD), and has recently gained increased attention for incompressible CFD problems for structured and unstructured grids. Two main advantages stand out when compared with traditional methods such as the finite volume method (FVM) or the finite difference method (FDM): first, DG offers an arbitrary order of error convergence due to the polynomial local approximation of the solution field. A polynomial approximation of degree p provides a numerical discretization error of the order $\mathcal{O}(h^{p+1})$ for sufficiently smooth solutions, where h is a characteristic grid length. Secondly, regardless of the desired order of accuracy, any given cell of the grid only requires information from its immediate neighbors, allowing for efficient parallelization with minimal communication overhead. In contrast, more traditional schemes, such as the FVM, are usually limited to $\mathcal{O}(h^N)$ accuracy, with $N \leq 2$ for unstructured grids. Even for structured grids N is practically limited to low values due to the increasing stencil size for increasing N . Advantageously the DG method offers the locality of low-order schemes and the accuracy per degree of freedom of spectral schemes.

This is an open access article under the terms of the Creative Commons Attribution License, which permits use, distribution and reproduction in any medium, provided the original work is properly cited.

© 2021 The Authors. *International Journal for Numerical Methods in Fluids* published by John Wiley & Sons, Ltd.

In the context of CFD solvers, an important distinction is that between pressure-based and density-based solvers. Historically, pressure-based solvers have been used for incompressible flows, that is, flows with divergence-free velocity fields. On the other hand, density-based (also called fully compressible) solvers should, in theory, be able to solve flows in all Mach number ranges. However, in practice, as the Mach number approaches zero, density-based solvers experience efficiency and accuracy problems. These issues are mainly attributed to the acoustic effects in the flow, which tends to generate very stiff systems. None of these approaches are directly applicable to flows with varying density in the low-Mach limit.² It is possible, however, to extend existing incompressible and compressible codes so that they are capable of dealing with low Mach numbers.³ In this work an extension from a incompressible solver is presented.

There are numerous works in which the DG method has been used within the context of incompressible flows.⁴⁻⁷ However, there are not many publications in which the flow problem at low Mach numbers is addressed using a pressure-based solver. In the work by Klein et al.⁸ the low-Mach equations are solved in a DG Framework making use of a SIMPLE type scheme. The solution of a time-step involves an iterative process that requires multiple matrix assemblies and solutions. The obtained systems of equations are solved by means of fixed-point iterations, where relaxation factors are necessary to obtain convergence of the computations. In the work of Hennink et al.² a pressure-based solver for low-mach flows is presented. They solve the mass flux instead of the velocity as the primitive variable.

High order methods are very attractive for complex reacting fluid dynamical systems, where usually a high numerical resolution is necessary. Particularly for combustion problems, where large amounts of heat are released in rather small zones within the flow, the high number of elements required to resolve the resulting steep gradients could result in prohibitive calculation times even for simple problems. In particular the study of so-called diffusion flames—also known as nonpremixed flames—requires special consideration. In a diffusion flame, the reactants are initially spatially separated. For this kind of system, mixing plays a crucial role because reactants need to be brought together to the flame zone in order to maintain combustion. Many practical applications of diffusion flames consider deflagration flames,⁹ which are characterized by a small characteristic velocity compared to the speed of sound. The low-Mach approximation of the Navier–Stokes equations is often chosen for describing this kind of system. This approximation allows for the calculation of nonconstant density flows (such as temperature dependent density), while neglecting acoustic effects, thus dramatically reducing the required temporal resolution.¹⁰

In addition to the aforementioned compressibility effects, the need to accurately and efficiently represent the chemical reactions governing the combustion problem poses a major challenge. Generally speaking, to study the combustion process a detailed chemistry description is preferable. However, this is often impractical as it can be very computationally intensive. Stauch et al. investigated systems with detailed mechanism for methanol combustion, where 23 chemical species and 166 elementary reactions are involved,¹¹ and for n-heptane with 62 chemical species and 572 elementary reactions, and with detailed transport processes.¹² Because of their high complexity the mentioned works are restricted to simple one- or two-dimensional configurations, and to a small number of grid elements. If one is interested in more complex geometries or more complicated flow systems, the use of detailed kinetics can be prohibitive. Simplified kinetic models have been developed to overcome this difficulty. In the work of Westbrook et al.¹³ a one-step kinetic model is presented, where combustion is expressed as a single chemical reaction with a reaction rate given by an Arrhenius-type expression with constant parameters. Multistep chemical reaction models have also been developed, such as the four-step mechanism for methane combustion by Peters,¹⁴ or the three-step mechanism by Peters and Williams.¹⁵ Furthermore, extensions of one-step models exist, such as the one presented by Fernandez-Tarrazo et al.¹⁶ for hydrocarbon combustion with air, where kinetic parameters are correlated to the equivalence ratio in order to better describe characteristic flame properties for premixed and nonpremixed flames.

In the last decades several numerical investigations related to diffusion flames have been carried out. Burke and Schumann were the first ones to investigate the structure of diffusion flames by studying the flame jet problem.¹⁷ By assuming an infinitely fast chemical reaction they managed to predict flame properties fairly accurately. In the work of Smooke et al.¹⁸ a numerical simulation for a two-dimensional axisymmetric laminar diffusion jet with detailed chemistry was conducted and solved with Newton-type methods. In order to obtain adequate initial estimates for this problem, the solution of the problem for an infinitely fast chemistry was solved first. This idea was used in several works such as that by Keyes and Smooke¹⁹ for a counter diffusion flame, by Smooke²⁰ for a Tsuji-counterflow configuration and in the work by Dobbins et al.²¹ for an axisymmetric laminar jet diffusion flame with time dependent boundary conditions. In the work of Paxion²² unstructured multigrid solver for laminar flames with detailed chemistry is presented. A Krylov–Newton method was used for solving several flame configurations. A two-dimensional counter diffusion flame was calculated, and its results were compared with the one-dimensional self-similar solution of the equations.

The DG method has also been used for simulations of combustion, mainly within a fully compressible framework. In the work from Johnson et al.²³ the compressible Navier–Stokes equations are solved using a nodal DG scheme for combustion with complex chemistry and transport parameters. An hp-adaptive method is also presented, and shown to be useful for solving the ordinary differential equations used for describing the unsteady behavior of the system. Similarly in the work from Lv and Ihme²⁴ a DG solver for multicomponent chemically reacting flows, which solves the fully compressible Navier–Stokes equation, is presented. A hybrid-flux formulation is used, where a conservative Riemann solver is used for shock treatment, and a double-flux formulation is used in smooth regions. They show its applicability for nonreacting and reacting flows, particularly for systems characterized by high Mach numbers. On the other hand, the solution of combustion problems using the DG method in an incompressible framework is a topic that has not received much attention in the literature. This fact is the motivation of this article.

The system of equations obtained from the discretization of highly nonlinear systems can be very difficult to solve. Fixed-point iteration schemes have been used as a linearization strategy, as done by Klein et al.⁸ A major drawback of this approach is the highly problem dependent choice of under-relaxation factors. A much more robust strategy is the use of Newton type methods.^{25,26} Here, a problem-dependent factor is not needed. There is however a trade-off, because the Jacobian matrix has to be calculated, which can be computationally expensive. This approach has been used for combustion problems in numerous works. Karaa et al.²⁷ studied the axisymmetric laminar jet diffusion flame and investigated the behavior of a multigrid solver when using different preconditioners with a damped Newton algorithm. Shen et al.²⁸ investigated the use and efficiency of a Newton method coupled with the Bi-CGSTAB method for an axisymmetric laminar jet flame. They concluded that, in terms of computational cost, the steady-state solution is more efficiently obtained by directly solving the steady formulation of the equations, than by solving the transient Navier–Stokes equations until the steady state is reached.

It is well known that the Newton method shows the property of having quadratic convergence sufficiently close to the solution.²⁹ However, if the initial solution guess is not adequate, the method converge to a solution slowly, or may not even converge at all. For some highly nonlinear problems this is a significant issue. The so-called globalized Newton methods are used to overcome this problem by effectively increasing the area of convergence of the method. A popular globalized Newton method is the Newton–Dogleg method,³⁰ which is based on a trust-region technique.

In this article, a steady low-Mach pressure-based solver for the simulation of temperature dependent nonreactive and reactive flows using the discontinuous Galerkin method is presented. To the best of our knowledge, this is the first time that a pressure-based solver is used together with the DG method for solving the reactive low-Mach equations using the Newton–Dogleg method in a fully coupled manner. We focus in this study on two-dimensional configurations, but the ideas presented could be extended to three-dimensional systems. The one-step combustion model presented by Fernandez-Tarrazo et al.¹⁶ is used for describing the chemical reactions. In the present work we consider only methane combustion, but the one-step model could be used for other hydrocarbons as well. We choose this chemical model to obtain physically correct results for a wide range of applications, while avoiding the use of complex chemistry models. The discrete system of equations is solved by a globalized Newton method, by means of the Dogleg approach. In addition to the Newton–Dogleg method, a homotopy strategy is presented, which was found to be useful for obtaining solutions of steady state calculations of highly nonlinear problems. In order to find appropriate initial values for Newton's method in combustion applications, the concept of flame sheet estimates (i.e., the solution for infinitely fast chemistry) is used. Several benchmark cases are presented that allow us to validate our implementation. First we solve the differentially heated cavity problem, with which we intend to validate our implementation of the low-Mach solver for nonconstant density flows using the fully coupled solver. Later two flame configurations are calculated, namely the counter-diffusion flame and the chambered diffusion flame.³¹

2 | GOVERNING EQUATIONS

2.1 | The reactive Navier–Stokes equations

Combustion processes can be modeled by a system of nonlinear partial differential equations, namely the balance equations for total mass, momentum, energy and mass of individual species (usually expressed in terms of mass fractions). This system needs to be solved together with an equation of state and expressions for the transport properties as well as for the chemical reaction rates. The derivation of the governing equations can be found in the literature.^{9,32} In the following, we briefly present the main concepts. We consider in the following a two-dimensional system. However, the

methods shown in this work could be also used for three-dimensional problems. Throughout this article, variables with a hat sign, for example, $\hat{\rho}$ represent dimensional variables while the ones without it are nondimensional. In particular we consider a Newtonian fluid. We assume that Fick's law of diffusion is valid. Soret and Dufour as well as viscous heat dissipation and heat radiation effects are also neglected, as they are only needed for special cases.³³ The energy equation is written in its temperature form, and the spatial gradients of the mixture heat capacity are assumed to be small. The enthalpy transport term due to diffusive fluxes have usually a small influence in the solution,^{22,34,35} and is neglected in the energy equation. Under these assumptions, the Navier–Stokes equations, the energy equation (in its temperature form) and the species transport equations are

$$\frac{\partial \hat{\rho}}{\partial \hat{t}} + \hat{\nabla} \cdot (\hat{\rho} \hat{\mathbf{u}}) = 0, \quad (1a)$$

$$\frac{\partial \hat{\rho} \hat{\mathbf{u}}}{\partial \hat{t}} + \hat{\nabla} \cdot (\hat{\rho} \hat{\mathbf{u}} \otimes \hat{\mathbf{u}}) = -\hat{\nabla} \hat{p} + \hat{\nabla} \cdot \left(\hat{\mu} \left(\hat{\nabla} \hat{\mathbf{u}} + (\hat{\nabla} \hat{\mathbf{u}})^T - \frac{2}{3} (\hat{\nabla} \cdot \hat{\mathbf{u}}) \mathbf{I} \right) \right) - \hat{\rho} \hat{\mathbf{g}}, \quad (1b)$$

$$\frac{\partial \hat{\rho} \hat{T}}{\partial \hat{t}} + \hat{\nabla} \cdot (\hat{\rho} \hat{\mathbf{u}} \hat{T}) = \frac{1}{\hat{c}_p} \frac{D \hat{p}}{D t} + \hat{\nabla} \cdot \left(\frac{\hat{k}}{\hat{c}_p} \hat{\nabla} \hat{T} \right) + \frac{\hat{Q} \hat{\omega}}{\hat{c}_p}, \quad (1c)$$

$$\frac{\partial \hat{\rho} Y_\alpha}{\partial \hat{t}} + \hat{\nabla} \cdot (\hat{\rho} \hat{\mathbf{u}} Y_\alpha) = \hat{\nabla} \cdot (\hat{\rho} \hat{D}_\alpha \hat{\nabla} Y_\alpha) + \nu_\alpha \hat{M}_\alpha \hat{\omega}, \quad (\alpha = 1, \dots, n_s - 1). \quad (1d)$$

Using the fact that the sum of the mass fractions must always be one, we can calculate the mass fraction Y_{n_s} as

$$Y_{n_s} = 1 - \sum_{\alpha=1}^{n_s-1} Y_\alpha. \quad (2)$$

Here ν_α and \hat{M}_α correspond to the stoichiometric coefficient and molecular weight of species α and n_s is the total number of species present in the system. The $\hat{\omega}$ and \hat{Q} parameters correspond to the global reaction rate and heat release respectively, and their definitions are given in Section 2.1.1. Additionally expressions for the density $\hat{\rho}$, mixture heat capacity \hat{c}_p and species transport have to be given. Assuming that the gas behaves ideally, the density can be calculated as

$$\hat{\rho}(\hat{p}, \hat{T}, \mathbf{Y}) = \frac{\hat{p}}{\mathcal{R} \hat{T} \sum_{\alpha=1}^{n_s} \frac{Y_\alpha}{\hat{M}_\alpha}}, \quad (3)$$

where \mathcal{R} is the ideal gas constant. Note that in Equation (3), the density is a function of the local composition, the temperature and the pressure. For an ideal mixture the specific heat capacity can be calculated as

$$\hat{c}_p(\hat{T}, \mathbf{Y}) = \sum_{\alpha=1}^{n_s} Y_\alpha \hat{c}_{p,\alpha}(\hat{T}), \quad (4)$$

where $\hat{c}_{p,\alpha}$ corresponds to the specific heat capacity of component α . The temperature dependency of $\hat{c}_{p,\alpha}$ is accounted by using NASA-polynomials.³⁶ The temperature dependence of the transport variables is calculated using Sutherland's law³⁷

$$\hat{\mu}(\hat{T}) = \hat{\mu}_{\text{suth}} \left(\frac{\hat{T}}{\hat{T}_{\text{suth}}} \right)^{1.5} \frac{\hat{T}_{\text{suth}} + \hat{S}}{\hat{T} + \hat{S}}. \quad (5)$$

Here $\hat{\mu}_{\text{suth}}$ is the viscosity evaluated at a reference temperature \hat{T}_{suth} , and \hat{S} is a material dependent parameter. Finally, by assuming constant values for the Prandtl and Lewis numbers (to be defined later), we obtain expression for the temperature dependency of the other transport parameters as $\hat{k}/\hat{c}_p(\hat{T}) = \hat{\mu}/\text{Pr}$ and $\hat{\rho} \hat{D}_\alpha(\hat{T}) = \hat{\mu}/\text{Pr} \text{Le}_\alpha$.

2.1.1 | Chemical model

In this article, we use the one-step kinetic model for hydrocarbon combustion presented from Fernandez-Tarrazo et al.¹⁶ The chemical reaction for a methane-air flame is represented by an exothermic global irreversible expression,

$\text{CH}_4 + 2\text{O}_2 \rightarrow \text{CO}_2 + 2\text{H}_2\text{O}$. The reaction releases a heat amount \hat{Q} . The reaction rate $\hat{\omega}$ appearing in the temperature and mass fraction equations is modeled as an Arrhenius type expression

$$\hat{\omega}(T, \mathbf{Y}) = \hat{B} \left(\frac{\hat{\rho} Y_F}{\hat{M}_F} \right)^a \left(\frac{\hat{\rho} Y_O}{\hat{M}_O} \right)^b \exp \left(-\frac{\hat{T}_a}{\hat{T}} \right). \quad (6)$$

Here the subscripts F and O refer to the fuel and oxidizer, respectively. The parameter $\hat{B} = 6.9 \times 10^{14} \text{ cm}^3/(\text{mol s})$ corresponds to the pre-exponential factor, \hat{T}_a is the activation temperature, and a and b are reaction orders. Within the model, several parameters are adjusted to represent characteristic features of premixed flames and diffusion flames. Fernandez-Tarrazo et al. define the parameters \hat{T}_a and \hat{Q} as functions of the local equivalence ratio ϕ , which is in turn defined in terms of the local mass fractions of fuel Y_F and oxidizer Y_O as

$$\phi(Y_F, Y_O) = \frac{s Y_F^0}{Y_O^0} \frac{s Y_F - Y_O + Y_O^0}{s(Y_F^0 - Y_F) + Y_O}, \quad (7)$$

where Y_F^0 and Y_O^0 are the mass fractions of fuel and oxidizer flows in their corresponding feed streams, and s is the mass stoichiometric ratio, defined as $s = \nu_O \hat{M}_O / \nu_F \hat{M}_F$. For methane combustion $s = 4$. The activation energy \hat{T}_a is also shown to be dependent on ϕ as

$$\hat{T}_a(\phi) = \begin{cases} (1 + 8.250(\phi - 0.64)^2) \hat{T}_{a0} & \text{if } \phi \leq 0.64, \\ \hat{T}_{a0} & \text{if } 0.64 \leq \phi \leq 1.07, \\ (1 + 4.443(\phi - 1.07)^2) \hat{T}_{a0} & \text{if } \phi \geq 1.07, \end{cases} \quad (8)$$

with $\hat{T}_{a0} = 15900 \text{ K}$. The reaction orders a and b are both set equal to one. Finally, The molar heat release is written as

$$\hat{Q}(\phi) = \begin{cases} \hat{Q}_0 & \text{if } \phi \leq 1 \\ (1 - \alpha(\phi - 1)) \hat{Q}_0 & \text{if } \phi > 1, \end{cases} \quad (9)$$

with $\hat{Q}_0 = 802.4 \text{ MJ kmol}^{-1}$ and $\alpha = 0.21$ for methane combustion. We note at this point that Equation (9) yields unphysical values of \hat{Q} for large values of ϕ . This problem can be avoided by setting an upper boundary value for ϕ in Equation (9) (we use $\phi = 1.2$). In practice however, this should not have a significant effect, because the unphysical values of \hat{Q} appear at zones where the reaction rate $\hat{\omega}$ is very close to zero, making the factor $\hat{Q}\hat{\omega}$ in the temperature equation negligible. Nevertheless, setting an upper bound for ϕ is helpful to avoid possible numerical instabilities.

2.2 | The steady nondimensional low-Mach equations

In this article, the low-Mach number limit approximation of the governing equations is used. This approximation is often used for flows where the Mach number (defined as $\text{Ma} = \hat{u}_{\text{ref}}/\hat{c}$, where \hat{u}_{ref} is a characteristic flow velocity and \hat{c} the speed of sound) is small, which is usually the case in typical laminar combustion systems.²¹ For a comprehensive derivation of the low-Mach equations we refer to other works.^{10,38-40} One of the main results of the analysis is that for flows with a small Mach number the pressure can be decomposed as $\hat{p}(\hat{\mathbf{x}}, \hat{t}) = \hat{p}_0(\hat{t}) + \hat{p}_2(\hat{\mathbf{x}}, \hat{t})$. The spatially uniform term $\hat{p}_0(\hat{t})$ is called thermodynamic pressure, and only appears in the equation of state. For an open system it is constant and equal to the ambient pressure, while for a closed system (e.g., a system completely bounded by walls) it changes in order to ensure mass conservation, compare, Section 4.1. The perturbational term $\hat{p}_2(\hat{\mathbf{x}}, \hat{t})$ plays a similar role as the pressure in the classical incompressible formulation, and only appears in the momentum equations. Effectively this approximation allows density variations due to temperature differences, and decouples it from the hydrodynamic pressure. From now on we will drop the subindex of the hydrodynamic pressure \hat{p}_2 and we will refer to it simply as \hat{p} .

We use in this work a nondimensional formulation of the governing equations. We define the nondimensional quantities

$$\rho = \frac{\hat{\rho}}{\hat{\rho}_{\text{ref}}}, \quad p = \frac{\hat{p}}{\hat{p}_{\text{ref}}}, \quad \mathbf{u} = \frac{\hat{\mathbf{u}}}{\hat{u}_{\text{ref}}}, \quad T = \frac{\hat{T}}{\hat{T}_{\text{ref}}}, \quad c_p = \frac{\hat{c}_p}{\hat{c}_{p,\text{ref}}}, \quad M_\alpha = \frac{\hat{M}_\alpha}{\hat{M}_{\text{ref}}},$$

$$\mu = \frac{\hat{\mu}}{\hat{\mu}_{\text{ref}}}, \quad D_\alpha = \frac{\hat{D}_\alpha}{\hat{D}_{\alpha,\text{ref}}}, \quad k = \frac{\hat{k}}{\hat{k}_{\text{ref}}}, \quad \nabla = \frac{\hat{\nabla}}{\hat{L}_{\text{ref}}}, \quad t = \frac{\hat{t}}{\hat{t}_{\text{ref}}}, \quad \mathbf{g} = \frac{\hat{\mathbf{g}}}{\hat{g}_{\text{ref}}}, \quad Q = \frac{\hat{Q}}{\hat{Q}_0}.$$

Here \hat{u}_{ref} , \hat{L}_{ref} , \hat{p}_{ref} , \hat{t}_{ref} , and \hat{T}_{ref} are the reference velocity, length, pressure, time and temperature, respectively, and are equal to some characteristic value for the particular studied configuration. Additionally, \hat{g}_{ref} is the gravitational acceleration and \hat{M}_{ref} is a reference molecular weight. The reference transport properties $\hat{\mu}_{\text{ref}}$, \hat{k}_{ref} , $\hat{D}_{\alpha,\text{ref}}$, and the reference heat capacity of the mixture and $\hat{c}_{p,\text{ref}}$ are evaluated at the reference temperature \hat{T}_{ref} . Similarly, the reference density has to satisfy the equation of state, thus $\hat{\rho}_{\text{ref}} = \hat{p}_{\text{ref}}/(\mathcal{R}\hat{T}_{\text{ref}}\hat{M}_{\text{ref}})$. By introducing these definitions in the governing Equations (1a) and (1d) the nondimensional reactive low-Mach number set of equations are obtained. Since we are interested in the steady solution of the governing equations, all temporal derivatives vanish. Finally, the system of differential equations to be solved reads

$$\nabla \cdot (\rho \mathbf{u}) = 0, \quad (10a)$$

$$\nabla \cdot (\rho \mathbf{u} \otimes \mathbf{u}) = -\nabla p + \frac{1}{\text{Re}} \nabla \cdot \mu \left(\nabla \mathbf{u} + \nabla \mathbf{u}^T - \frac{2}{3} (\nabla \cdot \mathbf{u}) \mathbf{I} \right) - \frac{1}{\text{Fr}^2} \rho \frac{\mathbf{g}}{\|\mathbf{g}\|}, \quad (10b)$$

$$\nabla \cdot (\rho \mathbf{u} T) = \frac{1}{\text{Re Pr}} \nabla \cdot \left(\frac{k}{c_p} \nabla T \right) + \text{H Da} \frac{Q \dot{\omega}}{c_p}, \quad (10c)$$

$$\nabla \cdot (\rho \mathbf{u} Y_\alpha) = \frac{1}{\text{Re Pr Le}_\alpha} \nabla \cdot (\rho D \nabla Y_\alpha) + \text{Da} \nu_\alpha M_\alpha \dot{\omega}. \quad (\alpha = 1, \dots, n_s - 1). \quad (10d)$$

The n_s th component mass fraction Y_{n_s} is calculated using Equation (2). This system is solved for the primitive variables velocity $\mathbf{u} = (u_x, u_y)$, pressure p , temperature T and mass fractions $\mathbf{Y} = (Y_1, \dots, Y_{n_s})$. Six nondimensional factors arise from the nondimensionalization process:

$$\text{Re} = \frac{\hat{\rho}_{\text{ref}} \hat{u}_{\text{ref}} \hat{L}_{\text{ref}}}{\hat{\mu}_{\text{ref}}}, \quad \text{Fr} = \frac{\hat{u}_{\text{ref}}}{\sqrt{\hat{g}_{\text{ref}} \hat{L}_{\text{ref}}}}, \quad \text{Pr} = \frac{\hat{c}_{p,\text{ref}} \hat{\mu}_{\text{ref}}}{\hat{k}_{\text{ref}}}, \quad \text{Le}_\alpha = \frac{\hat{k}_{\text{ref}}}{\hat{\rho}_{\text{ref}} \hat{D}_{\alpha,\text{ref}} \hat{c}_{p,\text{ref}}}, \quad \text{Da} = \frac{\hat{B} \hat{L}_{\text{ref}} \hat{\rho}_{\text{ref}}}{\hat{M}_{\text{ref}} \hat{u}_{\text{ref}}}, \quad \text{H} = \frac{\hat{Q}_0}{\hat{M}_{\text{ref}} \hat{c}_{p,\text{ref}} \hat{T}_{\text{ref}}},$$

the first three are the Reynolds, Froude and Prandtl number respectively. Le_α is the Lewis number of species α . Finally Da and H are the Damköhler number and the nondimensional heat release respectively. The nondimensional reaction rate is

$$\dot{\omega}(T, \mathbf{Y}) = \left(\frac{\rho Y_F}{M_F} \right) \left(\frac{\rho Y_O}{M_O} \right) \exp \left(\frac{-T_a}{T} \right), \quad (11)$$

where $T_a = \hat{T}_a / \hat{T}_{\text{ref}}$. Furthermore, the nondimensional heat release is

$$Q(\phi) = \begin{cases} 1 & \text{if } \phi \leq 1 \\ (1 - \alpha(\phi - 1)) & \text{if } \phi > 1, \end{cases} \quad (12)$$

with ϕ evaluated according to Equation (7). In the low-Mach limit, the ideal gas equation depends on the thermodynamic pressure, temperature and mass fractions. It reads in its nondimensional form

$$\rho(p_0, T, \mathbf{Y}) = \frac{p_0}{T \sum_{\alpha=1}^{n_s} \frac{Y_\alpha}{M_\alpha}}. \quad (13)$$

Similarly, the nondimensional specific heat capacity of the mixture c_p is calculated as

$$c_p(T, \mathbf{Y}) = \sum_{\alpha=1}^{n_s} Y_\alpha c_{p,\alpha}(T), \quad (14)$$

and the nondimensional viscosity as

$$\mu(T) = T^{\frac{3}{2}} \frac{1 + \hat{S}}{\hat{T}_{\text{ref}} T + \hat{S}}. \quad (15)$$

As mentioned before, the model for the transport parameters can be simplified by assuming constant values for the Prandtl and Lewis numbers.³⁴ and we can write $\mu(T) = k/c_p(T) = \rho D_\alpha(T)$. In all calculations in this work the value of \hat{S} for air is used, $\hat{S} = 110.5$ K.

2.3 | The flame sheet approximation

Here we introduce the concept of the flame sheet approximation, which is used in our solution algorithm for solving the finite reaction rate system given by Equations (10a) to (10d). We follow the ideas proposed in the work from Keyes and Smooke,¹⁹ which are shown briefly here for the sake of completeness. Assuming that all species have the same constant heat capacity c_p and mass diffusion coefficient $D_\alpha = D$, that the Lewis number is unity for all species, and that combustion can be described by a single step chemical reaction, it is possible to obtain an equation for a scalar without source terms, by taking a linear combination of the energy Equation (10c) and mass fraction Equation (10d). A commonly used scalar is the mixture fraction z , which per definition is equal to unity in the fuel feed stream, and equal to zero in the oxidizer feed stream. Thus, the system of Equations (10a) to (10d) can be simplified to solving the low-Mach Navier–Stokes equations together with an equation for the passive scalar z :

$$\nabla \cdot (\rho \mathbf{u}) = 0, \quad (16a)$$

$$\nabla \cdot (\rho \mathbf{u} \otimes \mathbf{u}) = -\nabla p + \frac{1}{\text{Re}} \nabla \cdot \mu \left(\nabla \mathbf{u} + \nabla \mathbf{u}^T - \frac{2}{3} (\nabla \cdot \mathbf{u}) \mathbf{I} \right) - \frac{1}{\text{Fr}^2} \rho \frac{\mathbf{g}}{\|\mathbf{g}\|}, \quad (16b)$$

$$\nabla \cdot (\rho \mathbf{u} z) = \frac{1}{\text{Re Pr}} \nabla \cdot (\rho D \nabla z), \quad (16c)$$

which are solved together with the equation of state and expressions for the transport parameters. Note that the system is not closed, because ρ , μ and ρD are still functions of temperature and mass fractions. These fields can be related to the mixture fraction using the concept of the Burke–Schumann flame structure.¹⁷ In the case of an infinitely fast chemical reaction fuel and oxidizer cannot coexist. On one side of this sheet only oxidizer is found, and on the other side only fuel. The exact position of the flame sheet can be determined by finding the locus of points where both reactant mass fractions Y_F and Y_O meet in stoichiometric proportions, that is, the points where the mixture fraction $z = z_{st}$, with

$$z_{st} = \frac{Y_O^0}{Y_O^0 + s Y_F^0}, \quad (17)$$

where Y_O^0 is the mass fraction of oxidizer in the oxidizer inlet stream, and Y_F^0 is the mass fraction of fuel in the fuel inlet stream. The Burke–Schumann solution provides analytical expressions for temperature and mass fraction fields on either side of the flame sheet as function of the mixture fraction z (see, e.g., the textbook from Poinso and Veynante⁹ or the work from Keyes and Smooke¹⁹). The function $\mathcal{H}(z)$, defined by

$$\mathcal{H}(z) = \begin{cases} 1 & \text{if } z \geq z_{st} \\ 0 & \text{if } z < z_{st} \end{cases} \quad (18)$$

can be used for writing the expressions in a more compact notation. The temperature field is given by

$$T(z) = z T_F^0 + (1 - z) T_O^0 + \frac{Q Y_F^0}{c_p} \frac{1 - z}{z_{st} (1 - z_{st})} \mathcal{H}(z) + \frac{Q Y_F^0}{c_p} z (1 - \mathcal{H}(z)), \quad (19)$$

where T_F^0 and T_O^0 are the temperature of the fuel inlet stream and oxidizer inlet stream, respectively. The mass fraction field of fuel Y_F , oxidizer Y_O and product Y_P are

$$Y_F(z) = Y_F^0 \frac{z - z_{st}}{1 - z_{st}} \mathcal{H}(z), \quad (20)$$

$$Y_O(z) = Y_O^0 \frac{z_{st} - z}{z_{st}} (1 - \mathcal{H}(z)), \quad (21)$$

$$Y_P(z) = Y_O^0 \frac{M_P \nu_P}{M_O \nu_O} (1 - z) \mathcal{H}(z) + Y_F^0 \frac{M_P \nu_P}{M_F \nu_F} z (1 - \mathcal{H}(z)). \quad (22)$$

Finally, it is possible to obtain an expression for the mass fraction of some inert component Y_N . Assuming that the fuel and oxidizer inlet feeds are at most diluted with some inert species, we can write

$$Y_N(z) = (1 - Y_F^0)z + (1 - Y_O^0)(1 - z). \quad (23)$$

In order to avoid numerical problems with singularities caused by the sharp change around $z = z_{st}$, we use a regularized form of the function \mathcal{H} given by

$$\mathcal{H}(z) \approx \frac{1}{2} (1 + \tanh(\sigma(z - z_{st}))), \quad (24)$$

where the parameter σ dictates the sharpness of the transition at $z = z_{st}$. The use of this regularized form of \mathcal{H} results in practice on a spreading of the flame front, which eases the numerical calculation.⁴¹ Once the mixture fraction field z is obtained, the temperature and mass fraction fields are uniquely defined by Equations (19)–(24), which are used to evaluate the density and the transport properties. This coupling between variables and the associated nonlinear system leads to the need for an iterative solution scheme.

2.4 | Boundary conditions

The following boundary conditions are imposed for the resolution of the finite reaction rate system (Equations (10a) to (10d)) and for the flame sheet problem (Equations (16a) to (16c)).

$$\Gamma_D : \quad \mathbf{u} = \mathbf{u}_D, \quad T = T_D, \quad Y_\alpha = Y_{\alpha,D}, \quad z = z_D, \quad (25a)$$

$$\Gamma_{DW} : \quad \mathbf{u} = \mathbf{u}_D, \quad \nabla T \cdot \mathbf{n}_{\partial\Omega} = 0, \quad \nabla Y_\alpha \cdot \mathbf{n}_{\partial\Omega} = 0, \quad \nabla z \cdot \mathbf{n}_{\partial\Omega} = 0, \quad (25b)$$

$$\Gamma_N : \quad \left(-p\mathbf{I} + \left(\frac{\mu}{\text{Re}} (\nabla \mathbf{u} + (\nabla \mathbf{u})^T) - \frac{2}{3} \mu (\nabla \cdot \mathbf{u}) \mathbf{I} \right) \right) \cdot \mathbf{n}_{\partial\Omega} = 0, \quad \nabla T \cdot \mathbf{n}_{\partial\Omega} = 0, \quad \nabla Y_\alpha \cdot \mathbf{n}_{\partial\Omega} = 0, \quad \nabla z \cdot \mathbf{n}_{\partial\Omega} = 0, \quad (25c)$$

$$\Gamma_{ND} : \quad \left(-p\mathbf{I} + \left(\frac{\mu}{\text{Re}} (\nabla \mathbf{u} + (\nabla \mathbf{u})^T) - \frac{2}{3} \mu (\nabla \cdot \mathbf{u}) \mathbf{I} \right) \right) \cdot \mathbf{n}_{\partial\Omega} = 0, \quad T = T_D, \quad Y_\alpha = Y_{\alpha,D}, \quad z = z_D \quad (25d)$$

$$\Gamma_P : \quad \mathbf{u}(\mathbf{x}) = \mathbf{u}(\mathbf{x}'), \quad T(\mathbf{x}) = T(\mathbf{x}'), \quad Y_\alpha(\mathbf{x}) = Y_\alpha(\mathbf{x}'), \quad z(\mathbf{x}) = z(\mathbf{x}'), \quad (25e)$$

where α denotes the index from mass fractions $\alpha = (1, \dots, n_s - 1)$. The boundary Γ_D represents conditions for inlets and walls, with velocity, temperature, mass fractions and mixture fraction defined as Dirichlet boundary conditions. Boundaries Γ_{DW} are used to represent adiabatic walls, where velocity is given as a Dirichlet boundary condition, but with the gradients perpendicular to the wall of the transported scalars set to zero. The boundary Γ_N represent an outflow of the domain with homogeneous Neumann condition for all scalars. The boundary Γ_{ND} also represents an outlet boundary condition, but with Dirichlet boundary conditions for the scalars. Finally the boundaries Γ_P are periodic boundaries, where \mathbf{x} and \mathbf{x}' are periodic pairs in the domain.

3 | NUMERICAL METHOD

3.1 | Spatial discretization

We start by introducing some standard definitions and notations in the context of DG methods:^{42,43} We define a computational domain $\Omega \subset \mathbb{R}^2$ with a polygonal and simply connected boundary $\partial\Omega$. Our numerical grid is then defined by the set of nonoverlapping elements $\mathcal{K} = \{K_1, \dots, K_N\}$ with a characteristic mesh size h , so that Ω is the union of all elements, that is, $\Omega = \bigcup_{i=1}^N K_i$. We define $\Gamma = \bigcup_j \partial K_j$ as the union of all edges (internal edges and boundary edges) and $\Gamma_I = \Gamma \setminus \partial\Omega$ as the union of all interior edges. For each edge of Γ a normal field \mathbf{n}_Γ is defined. Particularly on $\partial\Omega$ is defined as an outer normal and $\mathbf{n}_\Gamma = \mathbf{n}_{\partial\Omega}$. For each field $\mathbf{u} \in C^0(\Omega \setminus \Gamma_I)$ we define \mathbf{u}^- and \mathbf{u}^+ , which describe the information in the interior and exterior sides of the cell:

$$\mathbf{u}^- = \lim_{\xi \searrow 0} \mathbf{u}(\mathbf{x} - \xi \mathbf{n}_\Gamma) \quad \text{for } \mathbf{x} \in \Gamma, \quad (26)$$

$$\mathbf{u}^+ = \lim_{\xi \searrow 0} \mathbf{u}(\mathbf{x} + \xi \mathbf{n}_\Gamma) \quad \text{for } \mathbf{x} \in \Gamma_I. \quad (27)$$

The jump and mean values of \mathbf{u} on inner edges Γ_I are defined as:

$$[[\mathbf{u}]] = \mathbf{u}^+ - \mathbf{u}^-, \quad (28)$$

$$\{\mathbf{u}\} = \frac{1}{2} (\mathbf{u}^- + \mathbf{u}^+). \quad (29)$$

while the jump and mean values on boundary edges $\partial\Omega$ are:

$$[[\mathbf{u}]] = \mathbf{u}^-, \quad (30)$$

$$\{\mathbf{u}\} = \mathbf{u}^-. \quad (31)$$

We define the broken polynomial space of total degree k as

$$\mathbb{P}_k(\mathcal{K}_h) = \{f \in L^2(\Omega); \forall K \in \mathcal{K} : f|_K \text{ is polynomial and } \deg(f|_K) \leq k\}. \quad (32)$$

Additionally for $u \in C^1(\Omega \setminus \Gamma)$ the broken gradient $\nabla_h u$ is defined as:

$$\nabla_h u = \begin{cases} 0 & \text{on } \Gamma \\ \nabla u & \text{elsewhere} \end{cases}. \quad (33)$$

The broken divergence $\nabla_h \cdot u$ is defined analogously. Finally, we define the function space for test and trial functions for D_v dependent variables:

$$\mathbb{V}_{\mathbf{k}} = \prod_{i=1}^{D_v} \mathbb{P}_{k_i}(K_h), \quad (34)$$

where $\mathbf{k} = (k_1, \dots, k_{D_v})$.

3.1.1 | Discontinuous Galerkin discretization of the finite reaction rate problem

We start by presenting the DG discretization of the finite reaction system defined by Equations (10a) to (10d). We define $\mathbf{Y}' = (Y_1, \dots, Y_{n_s-1})$ as the vector containing the first $(n_s - 1)$ mass fractions and $\mathbf{s} = (s_1, \dots, s_{n_s-1})$ as the vector containing the test functions for the first $(n_s - 1)$ mass fraction equations. The discretized form of Equations (10a) to (10d) is obtained by multiplying each equation by a test function, integrating it over an element K , applying integration by parts and finally

using an adequate numerical flux for each term. Note that the convective and diffusive terms of the temperature scalars T , mass fraction Y_α and mixture fraction z have the same form, so they share the same expression in their discretized form. In order to ensure the validity of the Ladyzenskaja-Babuška-Brezzi (or inf-sup) condition,⁴⁴ we use a mixed order formulation, where polynomials of order k for velocity, temperature and mass fractions, and of degree $k' = k - 1$ for pressure are used. Finally the discretized problem can be written as: find the numerical solution $(p_h, \mathbf{u}_h, T_h, \mathbf{Y}'_h) \in \mathbb{V}_k$ such that for all test functions $(q_h, \mathbf{v}_h, r_h, \mathbf{s}_h) \in \mathbb{V}_k$ we have:

$$C(\mathbf{u}_h, q_h, \rho(T_h, \mathbf{Y}_h)) = \mathcal{B}^1(q_h), \quad (35a)$$

$$\mathcal{U}^C(\mathbf{u}_h, \mathbf{u}_h, \mathbf{v}_h, \rho(T_h, \mathbf{Y}_h)) + \mathcal{U}^P(p_h, \mathbf{v}_h) + \frac{1}{\text{Re}} \mathcal{U}^D(\mathbf{u}_h, \mathbf{v}_h, \mu(T_h)) + \frac{1}{\text{Fr}^2} \mathcal{U}^S(\rho(T_h, \mathbf{Y}_h), \mathbf{v}_h) = \mathcal{B}^2(\mathbf{v}_h), \quad (35b)$$

$$\mathcal{S}^C(\mathbf{u}_h, T_h, r_h, \rho(T_h, \mathbf{Y}_h)) + \frac{1}{\text{Re Pr}} \mathcal{S}^D(T_h, r_h, k/c_p(T_h)) + \text{H Da } \mathcal{S}^S(r_h, Q(T_h, \mathbf{Y}_h), \dot{\omega}(T_h, \mathbf{Y}_h), c_p(T_h, \mathbf{Y}_h)) = \mathcal{B}^3(r_h), \quad (35c)$$

$$\mathcal{S}^C(\mathbf{u}_h, Y_{ah}, s_{ah}, \rho(T_h, \mathbf{Y}_h)) + \frac{1}{\text{Re Pr Le}_\alpha} \mathcal{S}^D(Y_{ah}, s_{ah}, \rho D_\alpha(T_h)) + \text{Da } \mathcal{M}_\alpha^S(s_{ah}, \dot{\omega}(T_h, \mathbf{Y}_h)) = \mathcal{B}^3(s_{ah}), \quad (35d)$$

where the index α takes values $\alpha = 1, \dots, (n_s - 1)$. The n_s th component mass fraction Y_{n_s} is calculated using Equation (2).

3.1.2 | Discontinuous Galerkin discretization of the flame sheet problem

Discretizing the flame sheet problem given by Equations (16a) to (16c) proceeds in a similar way. Due to the similarity of the mass fraction equation and the mixture fraction equation the discretization is analogous. Again, we use a mixed order formulation of polynomials of degree k for velocity and mixture fraction, and of degree $k - 1$ for pressure. The resulting problem reads: find the numerical solution $(p_h, \mathbf{u}_h, z_h) \in \mathbb{V}_k$ such that for all test functions $(q_h, \mathbf{v}_h, r_h) \in \mathbb{V}_k$ we have:

$$C(\mathbf{u}_h, q_h, \rho(z_h)) = \mathcal{B}^1(q_h), \quad (36a)$$

$$\mathcal{U}^C(\mathbf{w}_h, \mathbf{u}_h, \mathbf{v}_h, \rho(z_h)) + \mathcal{U}^P(p_h, \mathbf{v}_h) + \frac{1}{\text{Re}} \mathcal{U}^D(\mathbf{u}_h, \mathbf{v}_h, \mu(z_h)) + \frac{1}{\text{Fr}^2} \mathcal{U}^S(\rho(z), \mathbf{v}_h) = \mathcal{B}^2(\mathbf{v}_h), \quad (36b)$$

$$\mathcal{S}^C(\mathbf{u}_h, z_h, r_h, \rho(z_h)) + \frac{1}{\text{Re Pr}} \mathcal{S}^D(z_h, r_h, \rho D(z_h)) = \mathcal{B}^3(r_h). \quad (36c)$$

Note that density and transport parameters are dependent on the mixture fraction z . The evaluation of those parameters is done as mentioned in Section 2.3 and solved iteratively using a Newton–Dogleg type method as shown later in Section 3.2.2

3.1.3 | Definitions of nonlinear forms

We show in the following the nonlinear forms used in this work. Regarding the choice of fluxes, we follow the “best practices” known in literature for the incompressible Navier–Stokes equation. It is known^{45,46} that central difference fluxes for the pressure gradient and velocity divergence, combined with a coercive form for the viscous terms, for example, symmetric interior penalty, gives a stable discretization for the Stokes equation. Furthermore, it is known that for all kinds of convective terms, a numerical flux which transports information in characteristic direction, for example, Upwind, Lax-Friedrichs or Local-Lax-Friedrichs, must be used. We opted for the last one in our implementation, as it offers a good compromise between accuracy and stability.

Continuity equation

We use a central difference flux for the discretization of the continuity equation:

$$C(\mathbf{u}, q, \rho) = \oint_{\Gamma_\Gamma \cup \Gamma_N \cup \Gamma_{ND} \cup \Gamma_P} \{\rho \mathbf{u}\} \cdot \mathbf{n}_\Gamma \llbracket q \rrbracket dS - \int_\Omega \rho \mathbf{u} \cdot \nabla_h q dV. \quad (37)$$

The density in Equation (37) is evaluated as a function of the temperature and mass fractions using the equation of state (Equation (13)). The term B^1 on the right hand sides of Equation (35a) and (36a) contains the Dirichlet boundary conditions:

$$B^1(q) = - \oint_{\Gamma_D \cup \Gamma_{Dw}} q(\rho_D \mathbf{u}_D \cdot \mathbf{n}_\Gamma) \cdot dS. \quad (38)$$

The density at the boundary ρ_D is evaluated with Equation (13) using the corresponding Dirichlet values of temperature and mass fractions.

Momentum equations

The convective term of the momentum equations is discretized using a Lax-Friedrichs flux

$$\mathcal{U}^C(\mathbf{w}, \mathbf{u}, \mathbf{v}, \rho) = \oint_{\Gamma} \left(\{\rho \mathbf{u} \otimes \mathbf{w}\} \mathbf{n}_\Gamma + \frac{\gamma_1}{2} \llbracket \mathbf{u} \rrbracket \right) \cdot \llbracket \mathbf{v} \rrbracket dS - \int_{\Omega} (\rho \mathbf{u} \otimes \mathbf{w}) : \nabla_h \mathbf{v} dV. \quad (39)$$

The Lax-Friedrichs parameter γ_1 is calculated as⁸

$$\gamma_1 = \max \left\{ 2\bar{\rho}^+ |\bar{\mathbf{u}}^+ \cdot \mathbf{n}^+|, 2\bar{\rho}^- |\bar{\mathbf{u}}^- \cdot \mathbf{n}^-| \right\}, \quad (40)$$

where $\bar{\rho}_h^\pm$ and $\bar{\mathbf{u}}^\pm$ are the mean values of ρ^\pm and \mathbf{u}^\pm in K^\pm , respectively.

The pressure term is discretized by using a central difference flux

$$\mathcal{U}^P(p, \mathbf{v}) = \oint_{\Gamma \setminus \Gamma_N \setminus \Gamma_{ND}} \{p\} (\llbracket \mathbf{v} \rrbracket \cdot \mathbf{n}) dS - \int_{\Omega} p \nabla_h \cdot \mathbf{v} dV. \quad (41)$$

The diffusive term of the momentum equations is discretized using an symmetric interior penalty (SIP) formulation⁴⁷

$$\begin{aligned} \mathcal{U}^D(\mathbf{u}, \mathbf{v}, \mu) &= \int_{\Omega} \left(\mu \left((\nabla_h \mathbf{u}) + (\nabla_h \mathbf{u})^T - \frac{2}{3} (\nabla_h \cdot \mathbf{u}) \mathbf{I} \right) \right) : \nabla_h \mathbf{v} dV \\ &- \oint_{\Gamma \setminus \Gamma_N \setminus \Gamma_{ND}} \left(\left\{ \mu (\nabla_h \mathbf{u} + \nabla_h \mathbf{u}^T - \frac{2}{3} (\nabla_h \cdot \mathbf{u}) \mathbf{I}) \right\} \mathbf{n}_\Gamma \right) \cdot \llbracket \mathbf{v} \rrbracket - \left(\left\{ \mu (\nabla_h \mathbf{v} + \nabla_h \mathbf{v}^T - \frac{2}{3} (\nabla_h \cdot \mathbf{v}) \mathbf{I}) \right\} \mathbf{n}_\Gamma \right) \cdot \llbracket \mathbf{u} \rrbracket dS \\ &+ \oint_{\Gamma \setminus \Gamma_N \setminus \Gamma_{ND}} \eta \mu_{max} \llbracket \mathbf{u} \rrbracket \llbracket \mathbf{v} \rrbracket dS. \end{aligned} \quad (42)$$

The viscosity μ is evaluated as a function of temperature according to Equation (15) and $\mu_{max} = \max(\mu^+, \mu^-)$. Additionally η is the penalty term of the SIP formulation, which has to be chosen big enough to ensure coercivity of the form, but also as small as possible in order to not increase the condition number of the problem. The estimation of the penalty term is based on an expression of the form

$$\eta = \eta_0 \frac{A(\partial K)}{V(K)}, \quad (43)$$

where for a two-dimensional problem A is the perimeter and V the area of the element. Parameter η_0 is a safety factor and is set $\eta_0 = 4$ in all calculations. Further information on the determination of the penalty term can be found in the work by Hillewaert.⁴⁸ The source term arising due to body forces is:

$$\mathcal{U}^S(\rho, \mathbf{v}) = \int_{\Omega} \rho \frac{\mathbf{g}}{\|\mathbf{g}\|} \cdot \mathbf{v} dV. \quad (44)$$

The right hand sides of Equations (35b) and (36b) contain the information from Dirichlet boundary conditions:

$$B^2(\mathbf{v}) = - \oint_{\Gamma_D} \left((\rho \mathbf{u}_D \otimes \mathbf{u}_D) \mathbf{n}_\Gamma + \frac{\gamma_1}{2} \mathbf{u}_D \right) \cdot \mathbf{v} dS + \oint_{\Gamma_D} \mu_D \mathbf{u}_D \cdot (\nabla_h \mathbf{v} \mathbf{n}_\Gamma + \nabla_h \mathbf{v}^T \mathbf{n}_\Gamma - \eta \mathbf{v}) dS. \quad (45)$$

The Dirichlet viscosity value μ_D is calculated from Equation (15) using the Dirichlet values of the temperature at the boundary.

Scalar equations

Since the convective and diffusive term for the temperature, mass fractions and mixture fraction share a similar form, we summarize here their discretized expressions in terms of an arbitrary scalar X (corresponding to T in the energy equation, Y_α in the equation for species α and z for the mixture fraction equation) and transport parameter ξ (i.e., k/c_p in the energy equation, and (ρD) for the mass fraction and mixture fraction equations). The convective term of the scalars is discretized using a Lax-Friedrichs flux

$$S^C(\mathbf{u}, X, r, \rho) = \oint_{\Gamma} \left(\{\rho \mathbf{u} X\} \cdot \mathbf{n} + \frac{\gamma_2}{2} \llbracket X \rrbracket \right) \llbracket r \rrbracket dS - \int_{\Omega} (\rho \mathbf{u} X \cdot \nabla_h r) dV. \quad (46)$$

The Lax-Friedrichs parameter γ_2 is calculated as⁸

$$\gamma_2 = \max \left\{ \overline{\rho^+} |\overline{\mathbf{u}^+} \cdot \mathbf{n}^+|, \overline{\rho^-} |\overline{\mathbf{u}^-} \cdot \mathbf{n}^-| \right\}. \quad (47)$$

The diffusion term of scalars is discretized again with a SIP formulation:

$$S^D(X, r, \xi) = \int_{\Omega} (\xi \nabla_h X \cdot \nabla_h r) dV - \oint_{\Gamma \setminus \Gamma_N \setminus \Gamma_{ND}} \left(\{\xi \nabla_h X\} \cdot \mathbf{n} \llbracket r \rrbracket + \{\xi \nabla_h r\} \cdot \mathbf{n} \llbracket X \rrbracket - \eta \xi_{\max} \llbracket X \rrbracket \llbracket r \rrbracket \right) dS. \quad (48)$$

The transport parameter ξ is calculated as a function of temperature using Equation (15) and $\xi_{\max} = \max(\xi^+, \xi^-)$. The boundary condition term of the corresponding scalar equation is:

$$B^3(r) = - \oint_{\Gamma_D \cup \Gamma_{ND}} \left((\rho_D \mathbf{u}_D X_D) \cdot \mathbf{n}_\Gamma + \frac{\gamma_2}{2} X_D \right) r dS + \oint_{\Gamma_D \cup \Gamma_{ND}} \xi_D X_D (\nabla_h r \cdot \mathbf{n}_\Gamma - \eta r) dS. \quad (49)$$

Here, X_D is the Dirichlet value of the scalar X on boundaries and ξ_D is the corresponding transport parameter calculated, which is calculated with Equation (15) using the Dirichlet values of the temperature at the boundary. Finally, the volumetric source term of the energy and mass fraction equations are defined as follows:

$$S^S(r, Q, \dot{\omega}, c_p) = \int_{\Omega} \frac{Q \dot{\omega}}{c_p} r dV, \quad (50)$$

$$\mathcal{M}_\alpha^S(s_\alpha, \dot{\omega}) = \int_{\Omega} \nu_\alpha M_\alpha \dot{\omega} s_\alpha dV. \quad (51)$$

The heat release Q is calculated with Equation (12), the reaction rate $\dot{\omega}$ is evaluated using Equation (11) and the mixture heat capacity with Equation (14).

3.2 | Computational methodology

The presented solver is embedded in the *BoSSS* (bounded support spectral solver) code, which is under development at the chair of fluid dynamics of the Technical University of Darmstadt, and is available under <https://github.com/FDYdarmstadt/BoSSS>. *BoSSS* is a general framework for the discretization of conservation laws using the DG method and uses a modal DG approach with orthonormal Legendre polynomials as basis functions. The *BoSSS* code features a variety of applications in the context of computational fluid dynamics, such as a solver for multiphase flows with a sharp interface approach,⁴² an incompressible Immersed boundary method solver for particle laden flows,⁴⁹ a solver for viscoelastic fluid flows,⁴³ and a solver for compressible flows,⁵⁰ among others.

The variational problem for the finite chemistry rate case described by Equations (35a) to (35d) and for the flame sheet problem, Equations (36a) to (36c), are linearized and solved using a Newton method with a Dogleg-type globalization.^{26,30} The *BoSSS* framework provides an efficient algorithm for the evaluation of the Jacobian based on perturbations of the

forms presented in the last section. The relatively large linear system of equations for each Newton iteration is solved by means of the in *BoSSS* integrated orthonormalization multigrid algorithm,⁵¹ which at the lowest multigrid levels makes use of the sparse direct solver PARDISO, originally developed by Schenk et al.,⁵²⁻⁵⁴ from the “Intel(R) Parallel Studio XE 2018 Update 3 Cluster Edition for Windows” library collection to solve the linear system.

BoSSS also features a method for solving highly nonlinear problems with a homotopy strategy. Further details on the used Newton method solver, the homotopy strategy and its implementation are given in the next sections, which are adapted from Kikker et al.⁴³ and are included for the sake of completeness. For information on the mentioned orthonormalization multigrid algorithm we refer the interested reader to the work of Kummer et al.⁵¹

3.2.1 | Calculation of the Jacobian matrix

We start by introducing a few new elements to be able to describe the implemented Newton method. The discussion for the variational problem using the mixture fraction variable (Equations (36a) to 36c) is completely analogous, and will not be mentioned in this discussions. The variational problem defined by Equations (35a) to (35d) can be cast into a more compact notation. By subtracting all terms from the right-hand sides from the terms of the left-hand sides of Equations (35a) to (35d) the problem can be written as: Find $\mathbf{U}_h \in \mathbb{V}_k$

$$\mathcal{N}(\mathbf{U}_h, \mathbf{V}_h) = 0 \quad \forall \mathbf{V}_h \in \mathbb{V}_k, \quad (52)$$

for $\mathbf{U}_h = (p_h, \mathbf{u}_h, T_h, \mathbf{Y}'_h)$ and $\mathbf{V}_h = (q_h, \mathbf{v}_h, r_h, \mathbf{s}_h)$. We assume a basis $\underline{\Phi} = (\Phi_1, \dots, \Phi_L)$ of \mathbb{V}_k , written as a row vector, with $L := \dim(\mathbb{V}_k)$. Then \mathbf{U}_h can be represented as $\mathbf{U}_h = \underline{\Phi} \cdot \mathbf{U}$. The nonlinear problem (52) can then be written as

$$\mathcal{A}(\mathbf{U}) = 0, \quad (53)$$

with the nonlinear function $\mathbb{R}^L \ni \mathbf{U} \mapsto \mathcal{A}(\mathbf{U}) \in \mathbb{R}^L$. The i th component of $\mathcal{A}(\mathbf{U})$, can be defined by $\mathcal{N}(-, -)$ through the relation $[\mathcal{A}(\mathbf{U})]_i = \mathcal{N}(\underline{\Phi} \cdot \mathbf{U}, \Phi_i)$.

The formulation of the Newton method requires the Jacobian matrix $\partial \mathcal{A}$ of \mathcal{A} , defined as

$$\partial \mathcal{A}_{ij}(\mathbf{U}) := \frac{\partial \mathcal{A}_i}{\partial U_j}(\mathbf{U}). \quad (54)$$

Its computation is quite straightforward, but lengthy. The *BoSSS* code is capable of evaluating the Jacobian matrix automatically from the expressions given in Section 3.1. We note that one could write $\mathcal{A}(\mathbf{U})$ as

$$[\mathcal{A}(\mathbf{U})]_i = \mathcal{N}(\mathbf{U}_h, \Phi_i) = \int_{\Omega_h} N_1(\mathbf{x}, \mathbf{U}_h, \nabla \mathbf{U}_h) \cdot \Phi_i + N_2(\mathbf{x}, \mathbf{U}_h, \nabla \mathbf{U}_h) \cdot \nabla \Phi_i dV + \oint_{\Gamma} \dots dS. \quad (55)$$

The edge integral, which is left out in Equation (55), can be written in analogous fashion as the volume integral, that is, as a sum over four nonlinear functions, multiplied by Φ_i^+ , Φ_i^- , $\nabla \Phi_i^+$ and $\nabla \Phi_i^-$, respectively. These functions themselves may depend on \mathbf{x} , \mathbf{U}_h^+ , \mathbf{U}_h^- , $\nabla \mathbf{U}_h^+$ and $\nabla \mathbf{U}_h^-$. For sake of compactness, this part is skipped. Realizing that $\frac{\partial \mathbf{U}_h}{\partial U_j} = \Phi_j$ and by application of the chain rule, one derives

$$\partial \mathcal{A}_{ij}(\mathbf{U}) = \int_{\Omega_h} (\partial_{\mathbf{U}_h} N_1(\mathbf{x}, \mathbf{U}_h, \nabla \mathbf{U}_h) \Phi_j + \partial_{\nabla \mathbf{U}_h} N_1(\mathbf{x}, \mathbf{U}_h, \nabla \mathbf{U}_h) \nabla \Phi_j) \cdot \Phi_i + \dots dV + \oint_{\Gamma} \dots dS. \quad (56)$$

All skipped terms in Equation (56) can be derived in an analogous fashion as the contributions for N_1 . In the *BoSSS* code, derivatives $\partial_{\mathbf{U}_h} N_1(\dots)$ and $\partial_{\nabla \mathbf{U}_h} N_1(\dots)$ are approximated by a finite difference, using a perturbation by $\sqrt{\text{eps}}$ in the respective argument, where $\text{eps} = 2.22044604925031 \cdot 10^{-16}$ is the floating point accuracy for double precision.

The notation introduced here allows us to describe the Newton–Dogleg method used in this work. We note however that this globalization strategy is still not sufficient to ensure convergence for some of the test cases presented, namely for high Rayleigh numbers for the differentially heated cavity problem. For those cases we use a homotopy strategy, where we start with a low homotopy-parameter, a parameter for which the solution of the problem is not hard to find, which

is gradually and carefully increased until convergence for the desired value of the homotopy-parameter is reached (cf. Section 3.3).

3.2.2 | Dogleg method

We consider a linearization of Equation (53) around \mathbf{U}_n ,

$$\mathcal{A}(\mathbf{U}_n) + \underbrace{\partial\mathcal{A}(\mathbf{U}_n)(\mathbf{U}_{n+1} - \mathbf{U}_n)}_{=: \mathbf{s}'_n} = 0. \quad (57)$$

By repeatedly solving this system one obtains a standard Newton scheme for Equation (53), yielding a sequence of approximate solutions $\mathbf{U}_0, \mathbf{U}_1, \mathbf{U}_2, \dots$ obtained from an initial guess \mathbf{U}_0 through the iteration scheme $\mathbf{U}_{n+1} = \mathbf{U}_n + \mathbf{s}'_n$. In the classical un-damped Newton method, the correction step \mathbf{s}'_n is set to be the whole Newton-step, that is, $\mathbf{s}'_n = \mathbf{s}_n$ with

$$\mathbf{s}_n := -\partial\mathcal{A}(\mathbf{U}_n)^{-1}\mathcal{A}(\mathbf{U}_n), \quad (58)$$

which is computed using a direct solver. Unfortunately, convergence of the Newton method for any starting value \mathbf{U}_0 is not guaranteed. In order to increase robustness when the distance between \mathbf{U}_0 and the exact solution \mathbf{U} is large, we employ a globalization approach, presented by Pawlowski et al.,^{26,30} known as the Dogleg-method, or Newton–Dogleg method. Here, we intend to give only the central ideas of method and refer to the original works for further details. Obviously, the exact solution of Equation (53) is also a minimum of the functional

$$f(\mathbf{U}) := \frac{1}{2}\|\mathcal{A}(\mathbf{U})\|_2^2. \quad (59)$$

One observes that $\nabla f(\mathbf{U}) = \partial\mathcal{A}(\mathbf{U})^T\mathcal{A}(\mathbf{U})$. For \mathbf{U}_n , the approximate Cauchy point with respect to the 2-norm, is defined as the minimizer \mathbf{g}_n of $\|\mathcal{A}(\mathbf{U}_n) + \partial\mathcal{A}(\mathbf{U}_n)\mathbf{g}_n\|_2$ in the direction of steepest decent, that is, $\mathbf{g}_n = \lambda\nabla f(\mathbf{U}_n)$, $\lambda \in \mathbb{R}$. Substituting $\mathbf{w} := -\partial\mathcal{A}(\mathbf{U}_n)\nabla f(\mathbf{U}_n)$, \mathbf{g}_n is given by

$$\mathbf{g}_n = \frac{\mathcal{A}(\mathbf{U}_n) \cdot \mathbf{w}}{\mathbf{w} \cdot \mathbf{w}}\nabla f(\mathbf{U}_n). \quad (60)$$

For the Newton–Dogleg method, the correction step \mathbf{s}'_n is chosen along the so-called Dogleg curve, which is the piece-wise linear curve from the origin to \mathbf{g}_n and further to \mathbf{s}_n . The selection of \mathbf{s}'_n on this curve is determined by the trust-region diameter $\delta > 0$:

- If $\|\mathbf{s}_n\|_2 \leq \delta$, $\mathbf{s}'_n = \mathbf{s}_n$.
- If $\|\mathbf{g}_n\|_2 \leq \delta$ and $\|\mathbf{s}_n\|_2 > \delta$, \mathbf{s}'_n is chosen on the linear interpolation from \mathbf{g}_n to \mathbf{s}_n so that $\|\mathbf{s}'_n\|_2 = \delta$: For the ansatz $\mathbf{s}'_n = \tau\mathbf{s}_n + (1 - \tau)\mathbf{g}_n$, the interpolation factor τ is given as $\tau = (a^2 - c + \sqrt{(a^2 + b^2 - 2c)\delta^2 - a^2b^2 + c^2})/(a^2 + b^2 - 2c)$ with $a = \|\mathbf{g}_n\|_2$, $b = \|\mathbf{s}_n\|_2$ and $c = \mathbf{g}_n \cdot \mathbf{s}_n$.
- If $\|\mathbf{g}_n\|_2 > \delta$, $\mathbf{g}_n = (\delta/\|\mathbf{g}_n\|_2)\mathbf{g}_n$.

The choice and adaptation of the trust region diameter δ throughout the Newton–Dogleg procedure follows a sophisticated heuristic, mainly based on comparing the actual residual reduction $\text{ared}_n := \|\mathcal{A}(\mathbf{U}_n)\|_2 - \|\mathcal{A}(\mathbf{U}_n + \mathbf{s}'_n)\|_2$ with the predicted residual reduction $\text{pred}_n := \|\mathcal{A}(\mathbf{U}_n)\|_2 - \|\mathcal{A}(\mathbf{U}_n) + \partial\mathcal{A}(\mathbf{U}_n)\mathbf{s}'_n\|_2$; For the direct solver used in this work pred_n simplifies to $\text{pred}_n := \|\mathcal{A}(\mathbf{U}_n)\|_2$. We replicate the algorithm here, for the sake of completeness:

- (1) Set $n = 0$, $\delta_n = \min(10^{10}, \max(2 \cdot 10^{-6}, \|\mathbf{s}_0\|_2))$.
- (2) Compute the Newton step \mathbf{s}_n and the Cauchy point \mathbf{g}_n and find \mathbf{s}'_n on the Dogleg curve with respect to the recent δ_n .
- (3) While $\text{ared}_n \leq \text{pred}_n$ do: Update trust region diameter $\delta_n \leftarrow 0.5 \delta_n$ and recompute \mathbf{s}'_n . If $\delta_n < 10^{-6}$ terminate abnormally and mark the computation as failed.
- (4) If the convergence criterion (see below) is fulfilled, terminate and mark the computation as success.

(5) Perform a final update of the trust region: Set

$$\delta_{n+1} = \begin{cases} \max(10^{-6}, \|\mathbf{s}_n\|_2) & \text{if } \text{ared}_n/\text{pred}_n < 0.1 \text{ and } \|\mathbf{s}_n\|_2\delta_n \\ \max(10^{-6}, 0.25 \cdot \delta_n) & \text{else, if } \text{ared}_n/\text{pred}_n < 0.1 \\ \min(10^{10}, 4 \cdot \delta_n) & \text{else, if } \text{ared}_n/\text{pred}_n > 0.75 \\ \delta_n & \text{otherwise} \end{cases}.$$

Set $\mathbf{U}_{n+1} = \mathbf{U}_n + \mathbf{s}'_n$, update $n \leftarrow n + 1$ and return to step (2).

All constants used in the algorithm above have been taken from the work of Pawlowski et al.²⁶ For a detailed description of the underlying ideas we also refer to these works, which in turn are based on algorithms from Dennis and Schnabel's textbook.⁵⁵

3.2.3 | Termination criterion

A simple approach to determine that a Newton–Dogleg loop can be terminated is to check whether the residual norm has fallen below a certain threshold, that is, $\|\mathcal{A}(\mathbf{U}_n)\| \leq \text{tol}$. A universal choice for the tolerance is indeed difficult, especially for investigations of convergence properties (cf. Sections 4.1.3 and 4.2.2). If it is chosen too low, the algorithm may never terminate, because of dominating numerical round-off errors. On the other hand, if it is chosen too high, the error of the premature termination may dominate the error of the spatial discretization and one cannot take the full advantage of the high-order method. Therefore the goal is to continue the Newton–Dogleg method until the lowest possible limit dictated by floating point accuracy is reached. To identify the limit in a robust way, we first define the residual-norm skyline as

$$\text{sr}_n := \min_{j \leq n} \|\mathcal{A}(\mathbf{U}_j)\| \quad (61)$$

and, for $n \geq 2$, the averaged reduction factor

$$\text{arf}_n := \frac{1}{2} \left(\frac{\text{sr}_{n-2}}{\max\{\text{sr}_{n-1}, 10^{-100}\}} + \frac{\text{sr}_{n-1}}{\max\{\text{sr}_n, 10^{-100}\}} \right). \quad (62)$$

The Newton–Dogleg method is terminated if

$$n \geq 2 \text{ and } \text{sr}_n \leq 10^{-5} + 10^{-5} \|\mathbf{U}_n\|_2 \text{ and } \text{arf}_n < 1.5. \quad (63)$$

For the computations in this work, this choice guarantees that the nonlinear system is solved as accurately as possible. It secures that the numerical error is dominated by the error of the spatial or temporal discretization and not by the termination criterion of the Newton–Dogleg method. The skyline approach ensures robustness against oscillations close to the lower limit.

3.3 | Homotopy method

Although the Newton–Dogleg method works well for a variety of cases, we experienced convergence problems for some of the test cases presented in next section. In particular, for the differentially heated cavity test case, the method was not successful on finding a convergent solution for a Rayleigh number $Ra \geq 10^5$ within 60 Newton iterations. In such cases we used a homotopy strategy, which is loosely based on ideas from the textbook of Deuflhard,²⁹ Chapter 5. We start by identifying a parameter that makes the solution of the nonlinear problem difficult to solve. In the following we will refer to this variable as the homotopy parameter. The main idea of the homotopy strategy consists of solving a series of simpler problems, starting with a parameter where the problem is easy to solve, and carefully increasing it until the desired value is reached. Let Hp denote the value of the homotopy parameter for which a solution is being

sought. Let

$$\mathcal{A}_{\text{hp}^*}(\mathbf{U}) = 0, \quad (64)$$

be the discretized system for a certain intermediate homotopy-parameter hp^* , between 0 and the “target” homotopy-parameter Hp , that is, $0 \leq \text{hp}^* \leq \text{Hp}$. Furthermore, let $\mathbf{U}_{\text{hp},\epsilon}$ be an approximate solution to the problem (64) with $\text{hp}^* = \text{hp}$, up to a tolerance ϵ , that is,

$$\|\mathcal{A}_{\text{hp}}(\mathbf{U}_{\text{hp},\epsilon})\|_2 \leq \epsilon. \quad (65)$$

For the sake of clarity when discussing the algorithm which follows below, we distinguish between the intermediate homotopy-parameter hp for which we assume to already have found an acceptable solution and the next homotopy-parameter hp^* that we are currently trying to find a solution for. For any $\text{hp}^* > \text{hp}$ we set $\epsilon = 10^{-5} \|\mathcal{A}_{\text{hp}^*}(\mathbf{U}_{\text{hp},\epsilon})\|_2$, that is, we aim for a residual norm reduction of at least five orders of magnitude with respect to the initial residual norm. If $\text{hp}^* = \text{Hp}$, the termination criterion presented in Section 3.2.3 is applied. An approximate solution for the target homotopy-parameter is found by the following recipe:

- (1) Set $\text{hp} = 0$, that is, start by obtaining an (approximate) solution $\mathbf{U}_{0,\epsilon}$.
- (2) Search for an increased homotopy-parameter hp^* : Find the minimal $i \geq 0$ so that for $\text{hp}^* = \frac{1}{2^i}(\text{Hp} - \text{hp}) + \text{hp}$ one has $\|\mathcal{A}_{\text{hp}^*}(\mathbf{U}_{\text{hp},\epsilon})\|_2 \leq \delta_{\text{max}} \|\mathcal{A}_{\text{hp}}(\mathbf{U}_{\text{hp},\epsilon})\|_2$. Here, δ_{max} is the maximal allowed increase of the residual for an increased homotopy-parameter hp^* ; δ_{max} is adapted in the following steps, as an initial guess we use $\delta_{\text{max}} = 10^6$.
- (3) Use the Newton–Dogleg method to compute an approximate solution to the problem (64), for the homotopy-parameter hp^* , using the solution $\mathbf{U}_{\text{hp},\epsilon}$ as an initial guess.
 - If the Newton–Dogleg method did not converge successfully within ten steps, the homotopy-parameter increase from hp to hp^* was probably too large. Set $\delta_{\text{max}} \leftarrow 0.2\delta_{\text{max}}$ and go to step (2).
 - If the Newton–Dogleg method reached its convergence criterion and if the target homotopy-parameter is reached, that is, $\text{hp}^* = \text{Hp}$, the algorithm has successfully found an approximate solution for $\mathcal{A}_{\text{Hp}}(\mathbf{U}) = 0$ and can terminate.
 - Otherwise, if the Newton–Dogleg method converged successfully, but is below the target homotopy-parameter: Accept the solution and set $\text{hp} \leftarrow \text{hp}^*$. If the Newton–Dogleg method took less than three iterations to reach the convergence criterion, set $\delta_{\text{max}} \leftarrow 8\delta_{\text{max}}$. Return to step (2).

An exemplary run of the method is shown in Figure 1. The homotopy parameter hp in this particular case is the Reynolds number. The homotopy-parameter hp was increased for iterations 10, 18, 22, and 24, causing an increase of the residuals $\|\mathcal{A}_{\text{hp}^*}(\mathbf{U}_n)\|_2$, leading to a convergent solution after 34 Newton iterations. The presented algorithm offers a robust method for finding steady-state solutions of highly nonlinear systems.

3.4 | Initialization of combustion applications

Cases involving combustion are initialized with the solution of the flame sheet problem, Equations (36a) to (36c). This idea has been already employed in various works.^{18,20} The reason for the use of this prestep is twofold:

- Solving Equations (10a) to (10d) using a Newton-type method requires adequate starting estimates in order to converge. Using the flame sheet solution as initial estimate improves the convergence properties of the method.
- The system of Equations (10a) to (10d) possesses multiple solutions. One is the pure mixing (frozen) solution, where no chemical reaction has taken place, and the other one is the ignited solution, where the flame is present. Using the flame sheet solution as initial estimate ensures that the path taken by Newton’s algorithm will tend toward the ignited solution.

We remark at this point that although for the solution of the flame sheet system the mixture heat capacity has been assumed to be constant, it remains an adequate estimate for the finite reaction-rate problem, where the heat capacity is a function of temperature and local concentration. In a similar fashion, the assumption of unity Lewis number in the flame sheet system delivers a solution that slightly deviates from the solution of the finite chemistry rate problem with

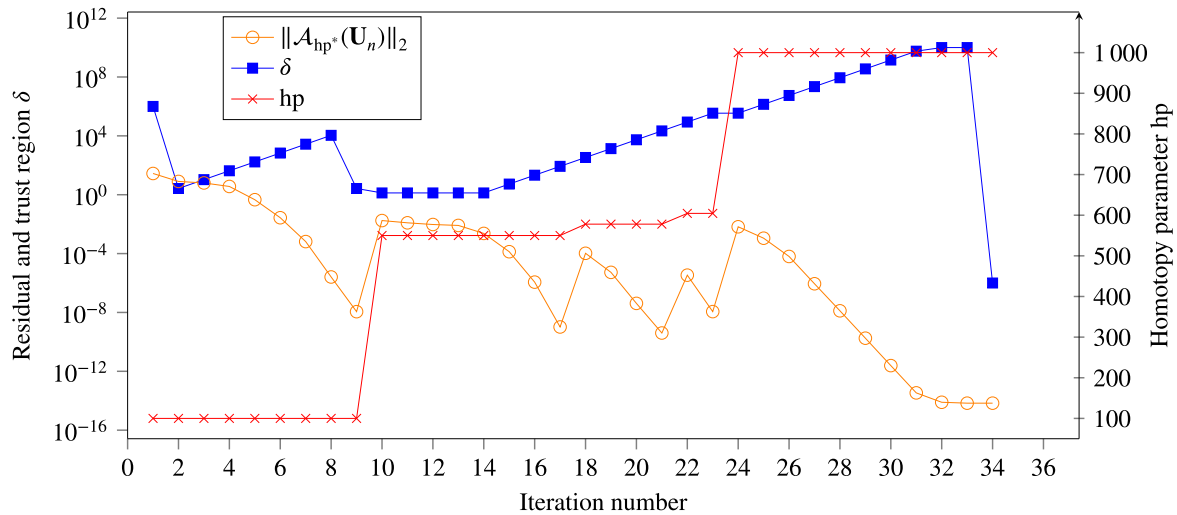


FIGURE 1 Behavior of the homotopy method for the differentially heated cavity test case. The homotopy parameter hp in this case is the Reynolds number [Colour figure can be viewed at wileyonlinelibrary.com]

nonunity Lewis numbers. Nevertheless, this small deviation does not preclude the use of the flame sheet solution as an adequate initial estimate for Newton's method, as will be shown in next sections.

4 | TEST CASES

The implemented solver for the reactive low-Mach equations is tested by solving several benchmark cases. In Section 4.1 we start by calculating a nonreactive case, namely the differentially heated cavity problem and the results are compared against a benchmark solution. Later, in Section 4.1.3 an h -convergence study using this configuration is done. Reactive cases are shown later. In Section 4.2.1 a two-dimensional flame in the counterflow configuration is calculated and the results compared with a one-dimensional self-similar solution of the flame. Finally in Section 4.2.2 a h -convergence study of the solver for a reactive case is presented.

4.1 | Differentially heated cavity problem

The differentially heated cavity problem corresponds to a classical benchmark case often used to assess the capability of numerical codes to simulate variable density flows.⁵⁶⁻⁵⁸ In this section, we show the basic set-up and compare our results with the ones presented in the work of Vierendeels et al.⁵⁷ where benchmark solutions for the differentially heated cavity are presented. They solve the fully compressible Navier–Stokes equations on a 1024×1024 stretched grid using a finite volume method with quadratic convergence.

The differentially heated cavity problem consists of a two-dimensional fully enclosed square cavity filled with fluid. A sketch of the problem is shown in Figure 2. The left and right walls of the cavity have a constant temperature \hat{T}_h and \hat{T}_c respectively, with $\hat{T}_h > \hat{T}_c$, and the top and bottom walls are adiabatic. A gravity field induces fluid movement due to the density differences caused by the difference of temperature between the hot and cold walls.

The natural convection phenomenon is characterized by the Rayleigh number, defined as

$$\text{Ra} = \text{Pr} \frac{\hat{g} \hat{\rho}_{\text{ref}}^2 (\hat{T}_h - \hat{T}_c) \hat{L}_{\text{ref}}^3}{\hat{T}_{\text{ref}} \hat{\mu}_{\text{ref}}^2}, \quad (66)$$

For small values of Ra, conduction dominates the heat transfer process, and a boundary layer covers the whole domain. On the other hand large values of Ra represent a convection dominated flow. For increasing Ra number, a thinner boundary layer is formed.

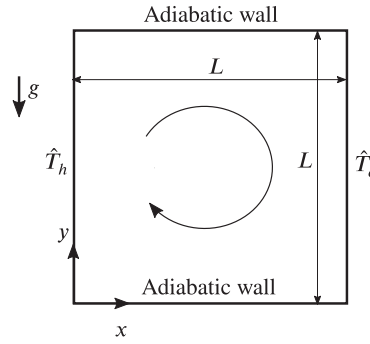


FIGURE 2 Schematic representation of the differentially heated cavity problem

4.1.1 | Set-up

A reference velocity for buoyancy driven flows can be defined as⁵⁷

$$\hat{u}_{\text{ref}} = \frac{\sqrt{\text{Ra}} \hat{\rho}_{\text{ref}}}{\hat{\rho}_{\text{ref}} \hat{L}_{\text{ref}}}. \quad (67)$$

The Rayleigh number is then related to the Reynolds number according to

$$\text{Re} = \sqrt{\text{Ra}}. \quad (68)$$

Thus it is sufficient to select a Re number in our simulation, fixing the value of the Ra number. The driving temperature difference ($\hat{T}_h - \hat{T}_c$) appearing in Equation (66) can be represented as an nondimensional parameter:

$$\varepsilon = \frac{\hat{T}_h - \hat{T}_c}{2\hat{T}_{\text{ref}}}. \quad (69)$$

Using these definitions, the Froude number can be calculated as

$$\text{Fr} = \sqrt{\text{Pr} 2\varepsilon}. \quad (70)$$

All calculations assume a constant Prandtl number equal to 0.71. The viscosity and heat conductivity dependence on temperature is calculated using Equation (15). Our results are calculated and compared with those of the reference solution for $\hat{T}_{\text{ref}} = 600$ K and $\varepsilon = 0.6$. The nondimensional length of the cavity is $L = 1$. The nondimensional temperatures T_h and T_c are set to 1.6 and 0.4, respectively. Since the cavity contains a single species, it is governed by the equations for continuity, momentum and temperature (Equations (10a) to (10c)) and no equation for species transport is needed. Thus $n_s = 1$ and $Y_1 = 1$ in the whole domain. Moreover, the nondimensional equation of state (Equation (13)) only depends on the temperature and reduces to

$$\rho = \frac{p_0}{T}. \quad (71)$$

The thermodynamic pressure p_0 in a closed system and has to be adapted in order to ensure mass conservation. If m_0 is the initial total mass of the system, the thermodynamic pressure is given by

$$p_0 = \frac{m_0}{\int_{\Omega} \frac{1}{T} dV}, \quad (72)$$

where Ω represents the complete closed domain. The initial mass of the system m_0 is constant and we set $m_0 = 1.0$. Within the solution algorithm, Equation (72) is used to update the value of the thermodynamic pressure after each

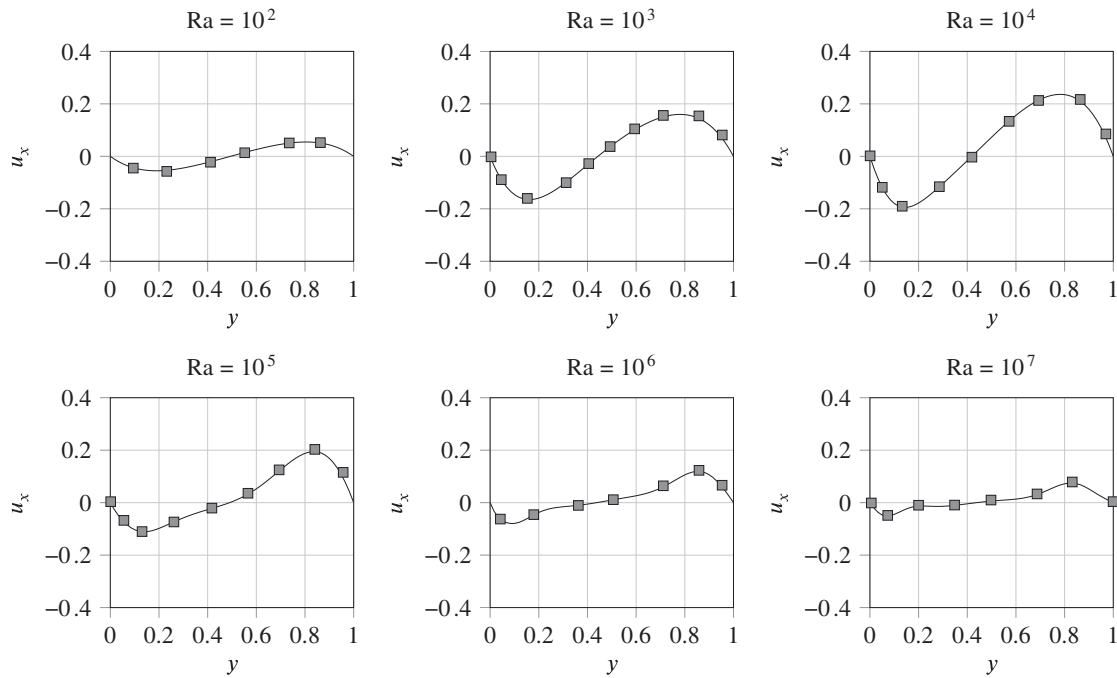


FIGURE 3 Profiles of the x-velocity component along the vertical line $x = 0.5$. Solid lines represents our solution and the marks the benchmark solution⁵⁷

Newton–Dogleg iteration. Moreover, the benchmark solution⁵⁷ also reports the Nusselt number and thermodynamic pressure associated with a given Rayleigh number. The Nusselt number is defined for a given wall Γ in its averaged form as

$$\text{Nu}_\Gamma = \frac{1}{T_h - T_c} \int_\Gamma k \frac{\partial T}{\partial x} dy. \quad (73)$$

4.1.2 | Comparison of results with benchmark solution

The benchmark results⁵⁷ are presented for $\text{Ra} = \{10^2, 10^3, 10^4, 10^5, 10^6, 10^7\}$. In this range of Rayleigh numbers the problem has a steady-state solution, thus we are able to use our steady formulation of the problem. The cavity is represented by the domain $[0, 1] \times [0, 1]$. We use an equidistant Cartesian mesh with 30×30 elements for each simulation. A polynomial degree of five is used for the velocities and temperature, and a degree of four for the pressure. It is observed that for cases until $\text{Ra} = 10^5$ the solution of the system using Newton’s method is possible without further modifications, while for higher values the algorithm diverges. The homotopy strategy mentioned in Section 3.2 is used to overcome this problem and obtain solutions for higher Rayleigh (and equivalently higher Reynolds) numbers. Here, the Reynolds number is selected as the homotopy parameter and continuously increased until the desired value is reached. In Figures 3–5 temperature and velocity profiles for different Rayleigh numbers are shown. The profiles calculated with *BoSSS* agree closely to the benchmark solution. As expected we observe an increase of the acceleration of the fluid in the vicinity of the walls for increasing Rayleigh numbers, forming a thin boundary layer. We also compare the thermodynamic pressure and the Nusselt numbers to the benchmark solution. The results are shown in Table 1. The thermodynamic pressure is obtained from Equation (72), and the Nusselt number is calculated with Equation (73). We observe that our results are in very good agreement with the reference results, and the thermodynamic pressure differ at most in the fourth decimal place. Note that the Nusselt number of the heated wall (Nu_h) and the Nusselt number of the cold wall (Nu_c) are different. As the Rayleigh number grows, this discrepancy becomes bigger, hinting that at such Rayleigh numbers the used mesh is not refined enough to represent adequately the thin boundary layer and more complex flow structures appearing at high-Rayleigh cases. While for an energy conservative system Nu_h and Nu_c should be equal, for our formulation this is not the case and the values differ slightly. This discrepancy can be seen as a measure of the discretization error from the

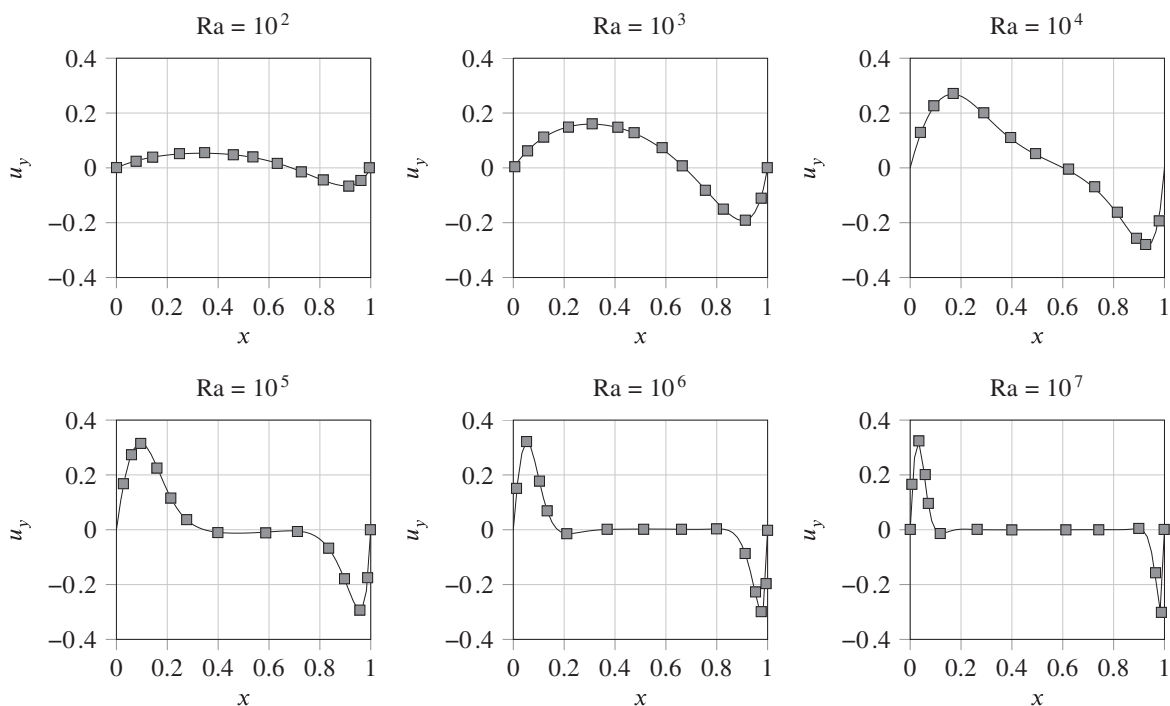


FIGURE 4 Profiles of the y-velocity component along the horizontal line $y = 0.5$. Solid lines represents our solution and marks the benchmark solution⁵⁷

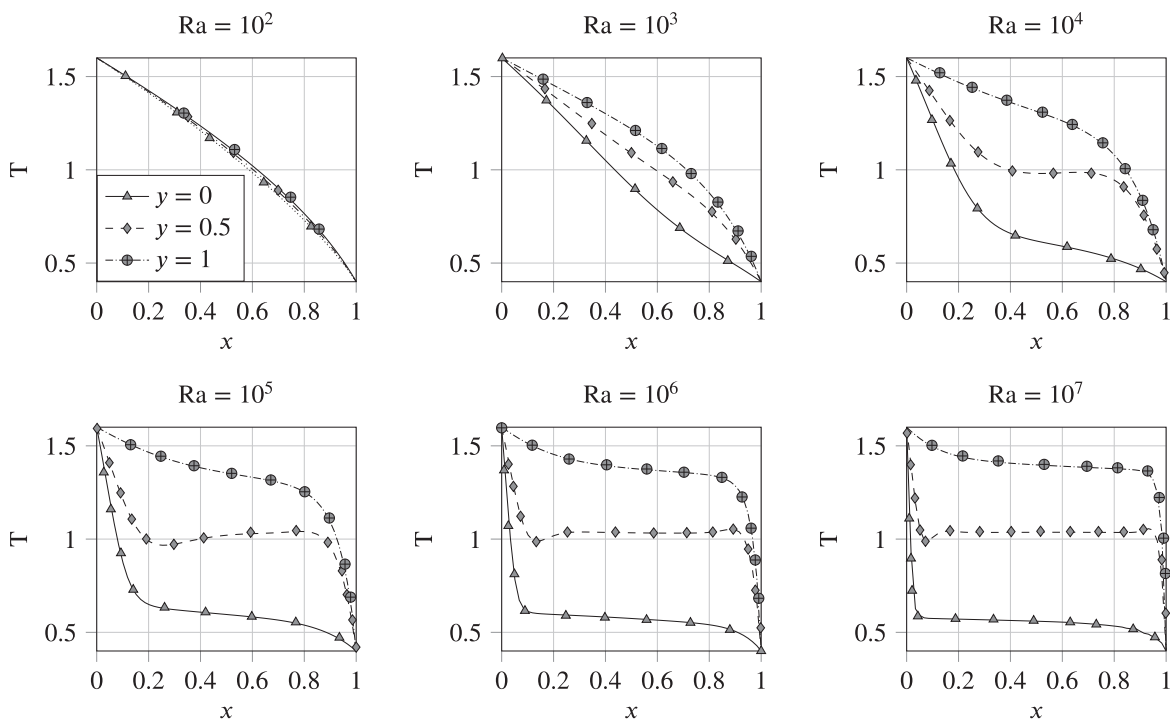


FIGURE 5 Temperature profiles for the differentially heated square cavity along different vertical levels. Solid lines represent our solution and marks the benchmark solution⁵⁷

TABLE 1 Comparison of calculated Nusselt numbers of the hot and cold wall and Thermodynamic pressure p_0 reported values⁵⁷ for the differentially heated cavity

Rayleigh	p_0	$p_{0,\text{ref}}$	Nu_h	Nu_c	Nu_{ref}
10^2	0.9574	0.9573	0.9787	0.9787	0.9787
10^3	0.9381	0.9381	1.1077	1.1077	1.1077
10^4	0.9146	0.9146	2.2180	2.2174	2.2180
10^5	0.9220	0.9220	4.4801	4.4796	4.4800
10^6	0.9245	0.9245	8.6866	8.6791	8.6870
10^7	0.9225	0.9226	16.2411	16.1700	16.2400

Note: Results are obtained for polynomial degree of four for the velocities and temperature, three for the pressure in an equidistant 128×128 mesh.

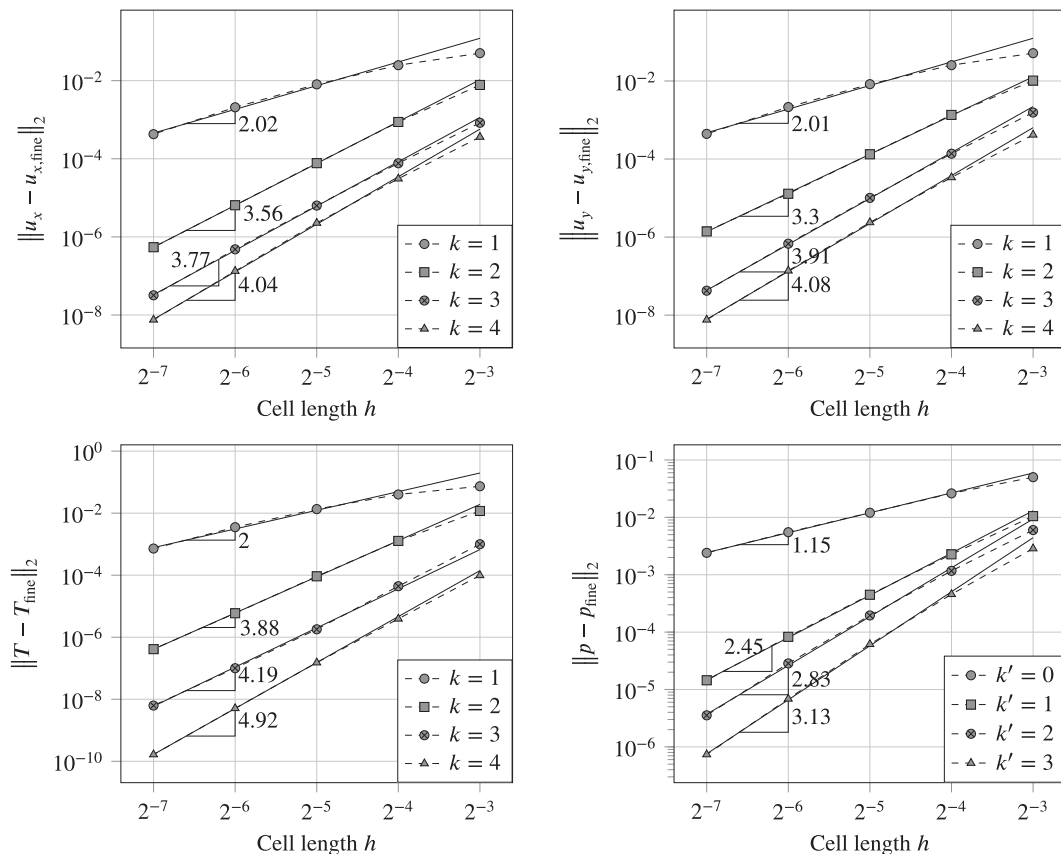


FIGURE 6 Convergence study of the differentially heated cavity problem for $Ra = 10^3$

DG formulation.⁸ This hints that the discrepancy between Nusselt numbers should decrease when increasing the mesh resolution, which will be discussed in the next section.

4.1.3 | Convergence study

An h -convergence study of the differentially heated cavity configuration was conducted. Calculations were done for polynomial degrees $k = 1, 2, 3, 4$ and equidistant regular meshes with respectively 8, 16, 32, 64, 128, and 256 elements in each spatial coordinate. The L^2 -Norm was used for the calculation of the errors against the solution on the finest mesh. Results of the h -convergence study for varying polynomial orders k are shown in Figure 6. Recall that for increasing polynomial order, the expected order of convergence is given by the slope of the line curve when cell length and errors are

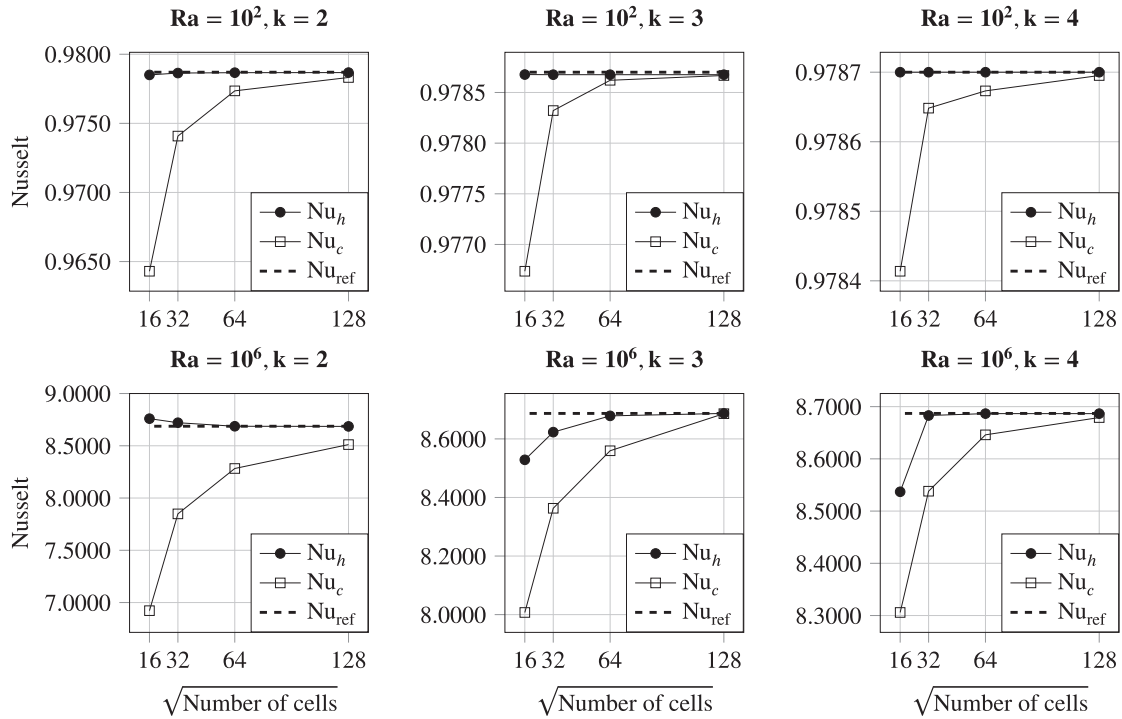


FIGURE 7 Nusselt numbers calculated with Equation (73) at the hot wall (Nu_h) and the cold wall (Nu_c) for different number of cells and polynomial order k . The reference values⁵⁷ are shown with dashed lines

presented in a log-log plot. Because we are using a mixed order formulation the slopes should be equal to k for the pressure and equal to $k + 1$ for all other variables. It is observed how convergence rates scale approximately as $k + 1$. Interestingly, for $k = 2$ the rates are higher than expected. On the other hand, some degeneration on the convergence rates is observed for $k = 4$.

As discussed in the last section, the difference on values of the Nusselt number on the hot wall Nu_h and the cold wall Nu_c is a consequence of spatial discretization error. In Figure 7 the convergence behavior of the Nusselt number for different polynomial degrees k , different number of elements and for two different Ra numbers is presented. As expected, it can be observed that this discrepancy is smaller when a higher number of elements is used.

4.2 | Combustion simulations

In the following, we show results of the simulations of two test cases with combustion, namely the counterflow diffusion flame and the chambered diffusion flame. For both cases, the solution of the flame sheet problem described in Section 2.3 is calculated first. This solution is used subsequently as initial estimates for the solution of the finite chemistry rate problem (cf. Section 2.2). In all test cases presented in this section, a smoothing parameter $\sigma = 50$ was used (cf. Section 2.3). For all test cases methane combustion according to the one-step model shown in Section 2.1.1 is considered. The mass fraction transport Equation (10d) is solved for the species CH_4 , O_2 , CO_2 and H_2O , thus $\mathbf{Y}' = (Y_{CH_4}, Y_2, Y_{CO_2}, Y_{H_2O})$. The nitrogen mass fraction Y_{N_2} is calculated according to Equation (2).

4.2.1 | Counterflow diffusion flame

The counterflow diffusion flame is a canonical configuration used to study the structure of nonpremixed flames. In its most basic configuration it consists of two oppositely situated jets. The fuel (possibly mixed with some inert component such as nitrogen) is fed into the system by one of the jets, while the other jet feeds air to the system, thereby establishing a stagnation point flow. Upon contact, the reactants produce a flame which is located in the vicinity of the stagnation plane.

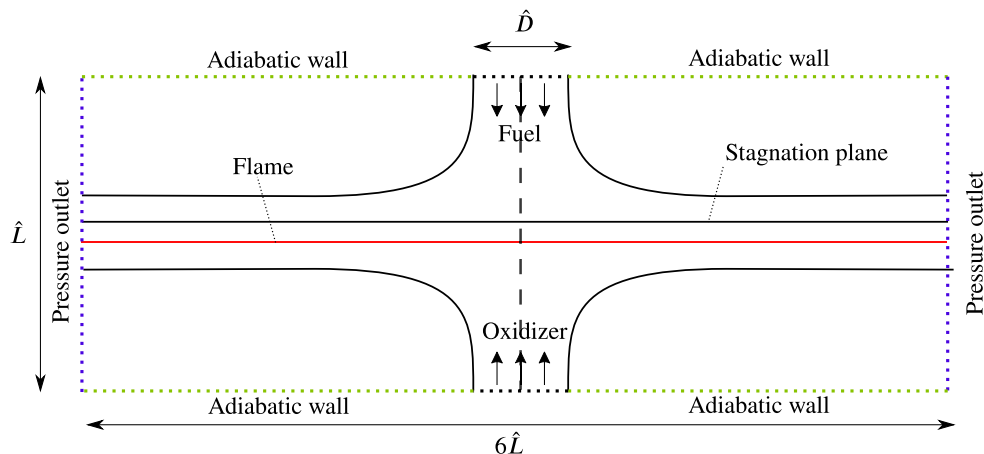


FIGURE 8 Schematic representation of the counterflow configuration [Colour figure can be viewed at wileyonlinelibrary.com]

A diagram of the setup can be seen in Figure 8. This simple configuration has been subject of study for decades because it provides a simple way of creating a strained diffusion flame, which proves to be useful when studying the flame structure, extinction limits or production of pollutants of flames.^{19,59,60} By assuming an infinite injector diameter and self-similarity of the solution, it is possible to reduce the governing equations to a one-dimensional formulation (see, e.g., the textbook of Kee³²). As a means of validating our implementation we compare the results with the solution of the one-dimensional self-similar problem calculated with BVP4, a fourth order finite difference boundary value problem solver provided by MATLAB.

The combustion of a methane-nitrogen mixture with air was simulated using the *BoSSScode*. The mass composition of the fuel inlet was assumed to be $Y_{\text{CH}_4}^0 = 0.2$ and $Y_{\text{N}_2}^0 = 0.8$, and the oxidizer inlet corresponds to air with $Y_{\text{O}_2}^0 = 0.23$ and $Y_{\text{N}_2}^0 = 0.77$. Because we are dealing with an open system, the thermodynamic pressure \hat{p}_0 is constant and set to the ambient pressure of 101325 Pa. As noted by Sung et al.,⁶¹ although the form of the inlet velocity profiles does have an influence on the solution of the problem, its effect on the solution near the flame zone is rather small. Nevertheless, as mentioned before the solution of the self-similar one-dimensional problem assumed an infinite injector diameter, which implies that the upstream velocity field has to be constant. Based on this fact we set the velocity profile of both inlets as a plug flow. Following combinations of inlet velocities were calculated:

- Low inlet velocities: $u_{\text{fuel}}^0 = 0.048 \text{ m s}^{-1}$ and $u_{\text{oxidizer}}^0 = 0.144 \text{ m s}^{-1}$,
- Medium inlet velocities: $u_{\text{fuel}}^0 = 0.12 \text{ m s}^{-1}$ and $u_{\text{oxidizer}}^0 = 0.36 \text{ m s}^{-1}$
- High inlet velocities: $u_{\text{fuel}}^0 = 0.24 \text{ m s}^{-1}$ and $u_{\text{oxidizer}}^0 = 0.72 \text{ m s}^{-1}$.

By using as definition of the strain rate the maximum axial velocity gradient, the calculated strains for the three cases mentioned above are 34 s^{-1} , 76 s^{-1} , and 155 s^{-1} , respectively. The temperature of both inlets is 300 K. The separation between both jets \hat{L} is equal to 0.02 m, and the length of the inlet opening \hat{D} is 0.02 m. The left and right domain boundaries are selected to be at a distance $3\hat{L}$ of the center. A nonunity but constant Lewis number formulation is used, with $\text{Le}_{\text{CH}_4} = 0.97$, $\text{Le}_{\text{O}_2} = 1.11$, $\text{Le}_{\text{H}_2\text{O}} = 0.83$, and $\text{Le}_{\text{CO}_2} = 1.39$.⁶² The heat capacity of each component is evaluated locally from NASA polynomials, and the mixture heat capacity is calculated with Equation (14).

In Figure 9 the convergence history obtained for a typical calculation of the counter diffusion flame is presented. The solution of the flame sheet calculation requires 17 iterations until convergence is reached. The obtained solution is used as a starting value for the finite chemical rate calculation, which only needs 10 iterations until convergence is reached. We note that because the flame sheet calculation is only used as an approximation of the final solution, a low polynomial degree can be used. For the flame sheet calculation $k = 2$ was chosen, resulting in a rather small system with 26,880 degrees of freedom. For the finite rate calculation $k = 4$ was used, which resulted in a system with 174,110 degrees of freedom. With the above-mentioned another advantage of the approach of using the flame sheet calculation for two-dimensional simulations can be highlighted. The initial estimate can be found relatively easily for a system with few degrees of freedom. Using the solution found as the initial estimate has the consequence that Newton's algorithm for the complete problem (which has many more degrees of freedom) only needs a few iterations to find a solution.

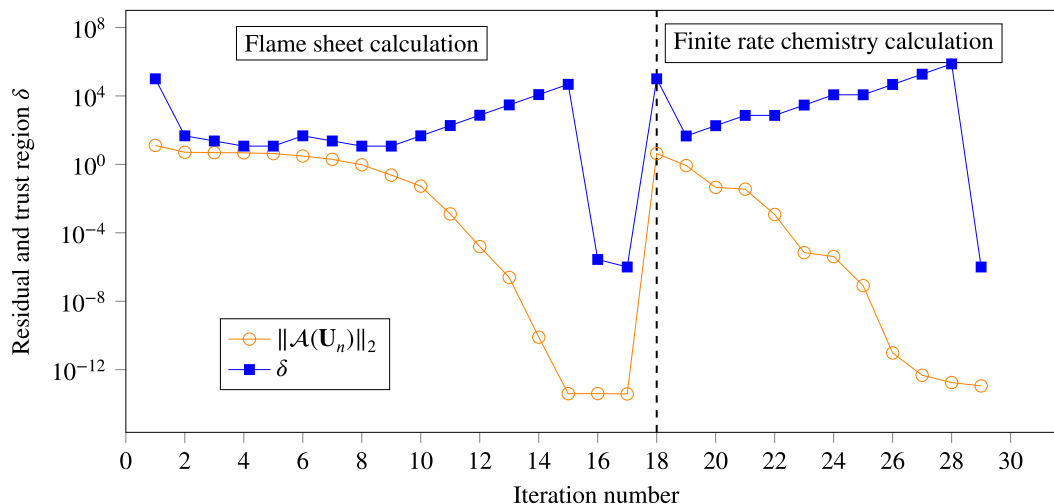


FIGURE 9 Convergence history of the diffusion flame in the counterflow configuration, with a maximum strain value of 165.1 s^{-1} [Colour figure can be viewed at wileyonlinelibrary.com]

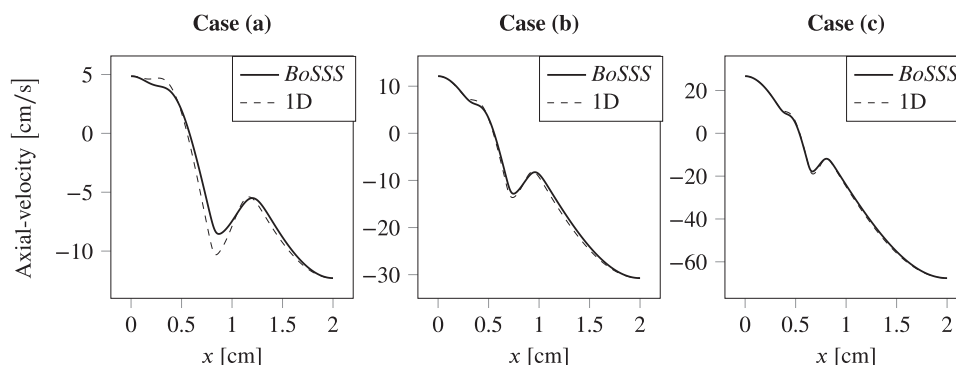


FIGURE 10 Comparison of the axial velocity calculated with *BoSSS* and the one-dimensional approximation

Because we are solving a two-dimensional configuration, in order to be able to compare our results with the ones obtained from the one-dimensional representation, the temperature, mass fractions and velocity profiles are extracted along the centerline of the system shown as the dashed line in Figure 8. In Figure 10 a comparison of the axial velocities calculated with *BoSSS* and the one-dimensional solution is shown. While for the high strain case the results agree closely, for lower strains a discrepancy is observed. Recall that the derivation of the one-dimensional approximation assumes a constant velocity field incoming to the flame zone in order to obtain a self-similar solution. In the case of the two-dimensional configuration presented here, the border effects do have an influence on the centerline, which disrupts the self-similarity. This effect is more pronounced for low velocities, which explains the discrepancy between curves. Similarly, In Figure 11 the temperature and mass fraction fields are presented. Again, a discrepancy is observed for low strains, but results show a good agreement for higher inlet velocities. It can also be observed how, as expected,¹⁶ at higher strains a significant penetration (leakage) of oxygen across the flame is present. Finally, in Figure 12 the two-dimensional temperature, velocity and reaction rate fields for the case (a) are shown. We note that the solution of this configuration showed singularities in the boundary points where the inlet and wall meet. This fact made hard to realize an h -convergence study for the complete domain. Based on this we decided to analyze a flame configuration that does not exhibit this behavior, as shown in the next section.

4.2.2 | Chambered diffusion flame

The chambered diffusion flame configuration has served as a model for many theoretical studies related to diffusion flames^{31,63,64} A scheme of the configuration can be seen in Figure 13. Fuel is injected at a constant rate into the bottom

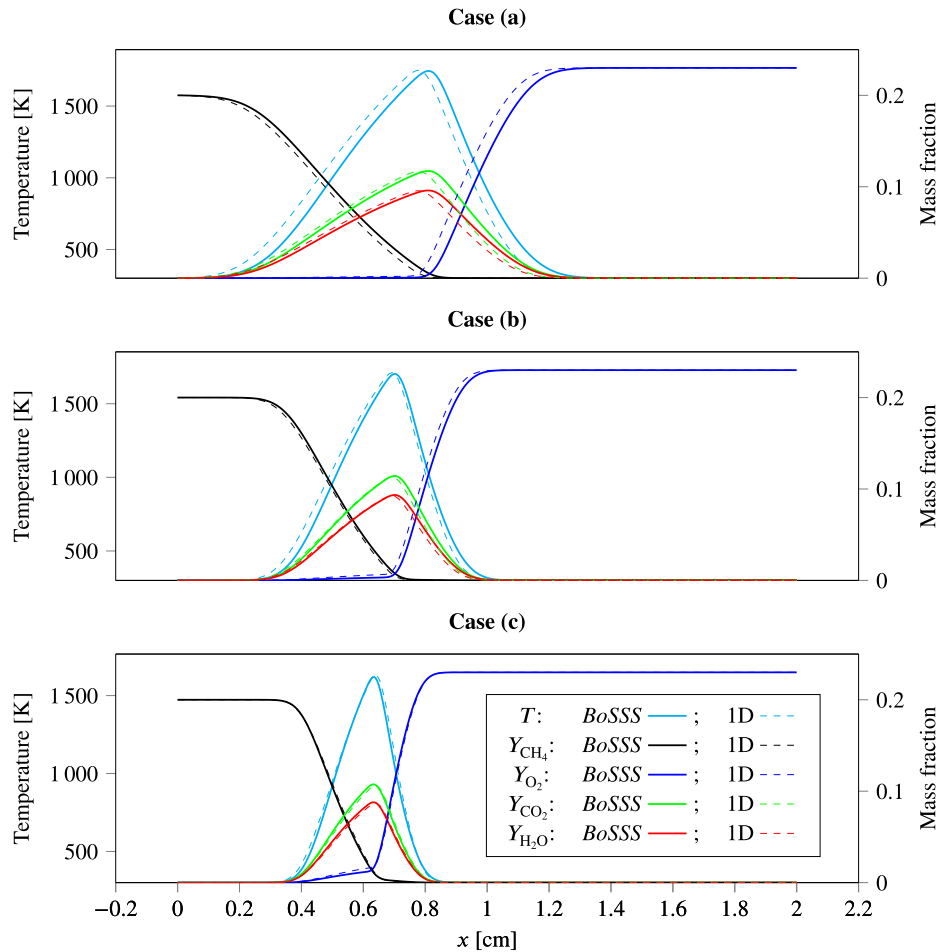


FIGURE 11 Comparison of temperature and mass fraction fields obtained with *BoSSS* and the one-dimensional approximation [Colour figure can be viewed at wileyonlinelibrary.com]

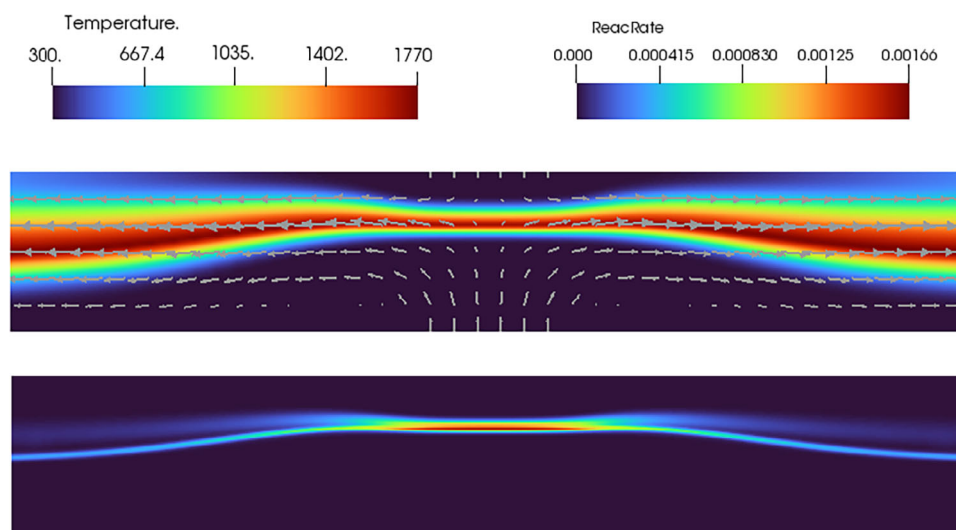


FIGURE 12 Calculated temperature and velocity fields (top picture) and reaction rate (second picture) of the counter diffusion flame configuration, case (a). The unit of the temperature is K and of the reaction rate $\text{kmol m}^{-3} \text{s}^{-1}$ [Colour figure can be viewed at wileyonlinelibrary.com]

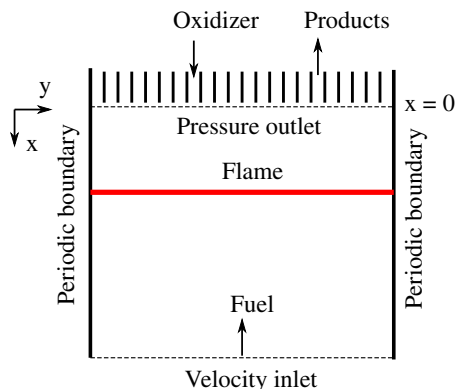


FIGURE 13 Schematic representation of the chambered diffusion flame configuration [Colour figure can be viewed at wileyonlinelibrary.com]

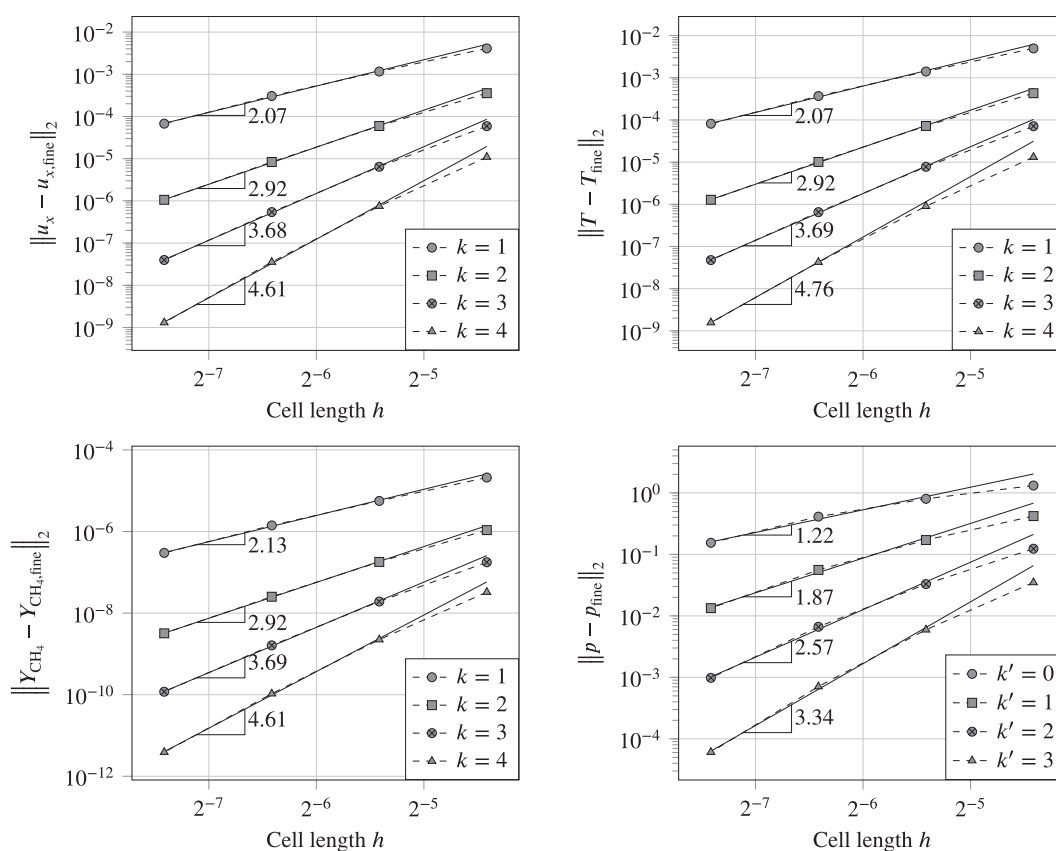


FIGURE 14 Convergence study for the chambered diffusion flame configuration

of a small insulated chamber, while oxidant diffuses into the system against the direction of flow. Constant conditions at the outlet of the chamber are achieved by a rapid renewal of the flow of oxidant. Under these conditions a planar flame forms far away from the walls, which allows a one-dimensional description of the flame structure. The fuel inlet into the chamber is modeled with a velocity inlet boundary condition Equation (25a), while the flow outlet at the top is considered an outlet as given by Equation (25d). Since we are interested in the flame in wall distance, it is sufficient to set the remaining boundary conditions as periodic boundaries. This effectively transforms the problem into a pseudo two-dimensional configuration.

In this test case we study the combustion of a $\text{CH}_4\text{-N}_2$ mixture with air. The thermodynamic pressure \hat{p}_0 is set equal to an ambient pressure of 101325 Pa. The inlet velocity of the fuel jet is set to 0.025 m s^{-1} and its mass composition is

$Y_{\text{CH}_4}^0 = 0.2$ and $Y_{\text{N}_2}^0 = 0.8$ while air has a composition $Y_{\text{O}_2}^0 = 0.23$ and $Y_{\text{N}_2}^0 = 0.77$. The temperature of the fuel and air feed streams is 300 K. The length of the system L is equal to 0.015 m. For this configuration an h -convergence study is conducted, where uniform Cartesian meshes with 5×2^6 , 5×2^7 , 5×2^8 , 5×2^9 , and 5×2^{10} cells are used. The polynomial degrees are varied from 1 to 4 for velocity, temperature and mass fractions, and from 0 to 3 for pressure. Errors are calculated using the finest mesh as a reference solution. The results are shown in Figure 14 for variables u_x , T , Y_{CH_4} and p . The convergence results for other variables are similar and not shown here. We observe the expected slope increase with increasing polynomial degrees. For low polynomial degrees the orders of convergence are very close to the theoretical values. However for higher polynomial degrees we observe a slight deterioration of the convergence rate.

5 | CONCLUSIONS

In this article, we have shown the discretization using the DG method for the reactive low-Mach equations. A mixed order formulation has been used, where velocity, temperature and mass fractions are represented by polynomials of degree k , and pressure by polynomials of degree $k - 1$. The system obtained from the discretization was solved by means of a Newton–Dogleg type method. Additionally, a homotopy strategy for solving highly nonlinear systems was introduced and used for some of the presented test cases. For the reactive test cases the concept of the flame sheet estimate was demonstrated to be a useful and computationally cheap way of initializing the finite reaction rate combustion calculations. The solver was used to calculate three different benchmark configurations, one without combustion and two cases with combustion. The first of these is the differentially heated cavity. This benchmark case was solved for varying Rayleigh numbers, spanning from $\text{Ra} = 10^2$ to $\text{Ra} = 10^7$. It was observed that for cases with Rayleigh number larger than 10^5 the use of our homotopy strategy was necessary to ensure convergence. Velocity and temperature profiles as well as thermodynamic pressure and Nusselt number were compared with a reference solution, obtaining very satisfactory results, thus validating our implementation of the method for variable density systems. An h -convergence study was presented for the differentially heated cavity, obtaining the expected convergence rates up to $k = 4$, where some degeneration on the rates was observed. Furthermore the counterflow diffusion flame configuration was analyzed, with which we intended to test the implemented chemistry model in conjunction with our solver. The results obtained with *BoSSS* were compared with results obtained by solving the self-similar one-dimensional representation of the counter diffusion flame configuration for varying strain rates. While for low strains some discrepancies between results were observed, the difference narrowed for high strains, which can be explained by the influence of the border effects on the centerline results for a two-dimensional configuration. Finally, the chambered diffusion flame configuration was used to study the convergence rates of our method. It was shown that, as expected, the convergence rates increase when using higher degree polynomials, but with some deterioration compared to the theoretical expected convergence. In future work the implemented solver is intended to be used in conjunction with our extended-DG solver^{42,49,51} in order to study multiphase reactive systems such as droplets.

ACKNOWLEDGMENTS

The work of Juan Gutierrez-Jorquera is funded by the Deutsche Forschungsgemeinschaft (DFG, German Research Foundation)—Project number: OB 96/47-1. The data that support the findings of this study are openly available in *TUdataLib* at <https://doi.org/10.48328/tudatalib-412>, Reference number.⁶⁵ Open access funding enabled and organized by Projekt DEAL.

NOMENCLATURE

Ma	Mach number
Re	Reynolds number
Pr	Prandtl number
Le	Lewis number
Da	Dahmköhler number
Fr	Froude number
Nu	Nusselt number
Ra	Rayleigh number
\mathbf{x}	Spatial coordinates vector
t	Time

u	Velocity vector
<i>t</i>	Time
<i>p</i>	Hydrodynamic pressure
<i>p</i> ₀	Thermodynamic pressure
g	Gravitational acceleration vector
<i>c_p</i>	Mixture heat capacity
<i>T</i>	Temperature
<i>Y_α</i>	Mass fraction of species <i>α</i>
<i>Q</i>	Molar heat release
<i>M_α</i>	Molecular weight of species <i>α</i>
<i>n_s</i>	Total number of species in the system
<i>L</i>	Length
<i>S</i>	Sutherland's law parameter
<i>B̂</i>	Pre-exponential factor of the one-step model
<i>q</i>	Molar heat of reaction
<i>z</i>	Mixture fraction
<i>s</i>	Mass stoichiometric ratio
<i>c</i>	Speed of sound
<i>M</i>	Molar mass
<i>ρ</i>	Density
<i>μ</i>	Viscosity
<i>λ</i>	Heat conductivity
<i>D</i>	Mass diffusivity
<i>ν</i>	Stoichiometric coefficient
<i>φ</i>	Local equivalence ratio
<i>κ</i>	Heat capacity ratio
<i>ω</i>	Reaction rate
<i>^</i>	Dimensional value
<i>F</i>	Fuel species
<i>O</i>	Oxidizer species
<i>P</i>	Product species
0	Initial value, zeroth order term from expansion
<i>α</i>	Species index
ref	Reference value
st	Stoichiometric proportions

DATA AVAILABILITY STATEMENT

The data that support the findings of this study are openly available in TUDatalib at <https://doi.org/10.48328/tudatalib-412>, Reference number.⁶⁵

ORCID

Juan Gutiérrez-Jorquera  <https://orcid.org/0000-0001-8593-5531>

REFERENCES

1. Cockburn B, Karniadakis GE, Shu C-W. The development of discontinuous Galerkin methods. In: Cockburn B, Karniadakis GE, Shu C-W, eds. *Discontinuous Galerkin Methods*. Lecture Notes in Computational Science and Engineering. Springer; 2000:3-50.
2. Hennink A, Tiberga M, Lathouwers D. A pressure-based solver for low-Mach number flow using a discontinuous Galerkin method. *J Comput Phys*. 2021;425:109877. doi:10.1016/j.jcp.2020.109877
3. Keshtiban I, Belblidia F, Webster M. Compressible flow solvers for low-Mach number flows— a review. *Int J Numer Methods Fluids*. 2003;23:2-5.
4. Shahbazi K, Fischer PF, Ethier CR. A high-order discontinuous Galerkin method for the unsteady incompressible Navier–Stokes equations. *J Comput Phys*. 2007;222(1):391-407. doi:10.1016/j.jcp.2006.07.029
5. Kummer F. *The BoSSS Discontinuous Galerkin Solver for Incompressible Fluid Dynamics and an Extension to Singular Equations*. Ph.D. thesis. Technische Universität Darmstadt; 2012.

6. Klein B, Kummer F, Oberlack M. A SIMPLE based discontinuous Galerkin solver for steady incompressible flows. *J Comput Phys*. 2013;237:235-250. doi:10.1016/j.jcp.2012.11.051
7. Rhebergen S, Cockburn B, van der Vegt JJW. A space– time discontinuous Galerkin method for the incompressible Navier–Stokes equations. *J Comput Phys*. 2013;233:339-358. doi:10.1016/j.jcp.2012.08.052
8. Klein B, Müller B, Kummer F, Oberlack M. A high-order discontinuous Galerkin solver for low-Mach number flows. *Int J Numer Methods Fluids*. 2016;81(8):489-520. doi:10.1002/flid.4193
9. Poinso T, Veynante D. *Theoretical and Numerical Combustion*. R.T. Edwards, Inc; 2005.
10. Müller B. Low-Mach-number asymptotics of the Navier-Stokes equations. *J Eng Math*. 1998;34(1):97-109. doi:10.1023/A:1004349817404
11. Stauch R, Lipp S, Maas U. Detailed numerical simulation of the auto-ignition of liquid fuel droplets. In: Shokin Y, Resch M, Shokina N, Danaev N, Orunkhanov M, eds. *Advances in High Performance Computing and Computational Sciences*. Springer; 2006:127-137.
12. Stauch R, Maas U. The auto-ignition of single n-heptane/iso-octane droplets. *Int J Heat Mass Transf*. 2007;50(15):3047-3053. doi:10.1016/j.ijheatmasstransfer.2006.12.005
13. Westbrook CK, Dryer FL. Simplified reaction mechanisms for the oxidation of hydrocarbon fuels in flames. *Combust Sci Technol*. 1981;27(1-2):31-43. doi:10.1080/00102208108946970
14. Peters N. Numerical and asymptotic analysis of systematically reduced reaction schemes for hydrocarbon flames. In: Glowinski R, Larrouturou B, Temam R, eds. *Numerical Simulation of Combustion Phenomena*. Lecture Notes in Physics. Springer; 1985:90-109.
15. Peters N, Williams FA. The asymptotic structure of stoichiometric methane-air flames. *Combust Flame*. 1987;68(2):185-207. doi:10.1016/0010-2180(87)90057-5
16. Fernandez-tarrazo E, Sanchez A, Linan A, Williams F. A simple one-step chemistry model for partially premixed hydrocarbon combustion. *Combust Flame*. 2006;147(1-2):32-38. doi:10.1016/j.combustflame.2006.08.001
17. Burke SP, Schumann TEW. Diffusion flames. *Ind Eng Chem*. 1928;20(10):998-1004. doi:10.1021/ie50226a005
18. Smooke MD, Mitchell RE, Keyes DE. Numerical solution of two-dimensional axisymmetric laminar diffusion flames. *Combust Sci Technol*. 1986;67(4-6):85-122. doi:10.1080/00102208908924063
19. Keyes DE, Smooke MD. Flame sheet starting estimates for counterflow diffusion flame problems. *J Comput Phys*. 1987;73(2):267-288. doi:10.1016/0021-9991(87)90137-9
20. Smooke MD, Giovangigli V. Numerical modeling of axisymmetric laminar diffusion flames. *IMPACT Comput Sci Eng*. 1992;4(1):46-79. doi:10.1016/0899-8248(92)90016-2
21. Dobbins RR, Smooke MD. A fully implicit, compact finite difference method for the numerical solution of unsteady laminar flames. *Flow Turbul Combust*. 2010;85(3-4):763-799. doi:10.1007/s10494-010-9278-z
22. Paxion S, Baron R, Gordner A, et al. Development of a parallel unstructured multi-grid solver for laminar flame simulations with detailed chemistry and transport. In: Hirschel EH, ed. *Numerical Flow Simulation II. Notes on Numerical Fluid Mechanics (NNFM)*. Springer; 2001:181-198.
23. Johnson RF, Kercher AD. A conservative discontinuous Galerkin discretization for the chemically reacting Navier-Stokes equations. *J Comput Phys*. 2020;423:109826. doi:10.1016/j.jcp.2020.109826
24. Lv Y, Ihme M. High-order discontinuous Galerkin method for applications to multicomponent and chemically reacting flows. *Acta Mech Sin*. 2017;33:1-14. doi:10.1007/s10409-017-0664-9
25. Shadid JN, Tuminaro RS, Walker HF. An inexact Newton method for fully coupled solution of the Navier–Stokes equations with heat and mass transport. *J Comput Phys*. 1997;137(1):155-185. doi:10.1006/jcph.1997.5798
26. Pawlowski RP, Shadid JN, Simonis JP, Walker HF. Globalization techniques for newton–Krylov methods and applications to the fully coupled solution of the Navier–Stokes equations. *SIAM Rev*. 2006;48(4):700-721. doi:10.1137/S0036144504443511
27. Karaa S, Zhang J, Douglas CC. Preconditioned multi-grid simulation of an axisymmetric laminar diffusion flame. *Math Comput Model*. 2003;38(3):269-279. doi:10.1016/S0895-7177(03)90086-0
28. Shen W, Zhang J, Yang F. Newton's method for steady and unsteady reacting flows. *ACM-SE 44*; 2006. 10.1145/1185448.1185621
29. Deufhard P. *Newton Methods for Nonlinear Problems*. Springer Series in Computational Mathematics. Springer; 2011.
30. Pawlowski RP, Simonis JP, Walker HF, Shadid JN. Inexact Newton Dogleg methods. *SIAM J Numer Anal*. 2008;46(4):2112-2132.
31. Matalon M, Ludford GSS, Buckmaster J. Diffusion flames in a chamber. In: Oppenheim AK, ed. *Gasdynamics of Explosions and Reactive Systems*. Pergamon; 1980:943-959.
32. Kee RJ, Coltrin ME, Glarborg P. *Chemically Reacting Flow: Theory and Practice*. Wiley-Interscience; 2003.
33. Bird RB, Stewart WE, Lightfoot EN. *Transport Phenomena*. Wiley; 1960.
34. Smoke MD, Giovangigli V. Formulation of the premixed and nonpremixed test problems. In: Smooke MD, ed. *Reduced Kinetic Mechanisms and Asymptotic Approximations for Methane-Air Flames: A Topical Volume*. Lecture Notes in Physics. Springer; 1991:1-28.
35. Goey P, Somers LMT, Bosch W, Mallens R. Modeling of the small scale structure of flat burner-stabilized flames. *Combust Sci Technol*. 1995;104:387-400. doi:10.1080/00102209508907729
36. McBride BJ, Gordon S, Reno MA. NASA thermodynamic data base. No. 4513 in NASA Technical Memorandum; 1993.
37. Sutherland W. LII. the viscosity of gases and molecular force. *Lond Edinburgh Dublin Philos Mag J Sci*. 1893;36(223):507-531. doi:10.1080/14786449308620508
38. Majda A, Sethian J. The derivation and numerical solution of the equations for zero Mach number combustion. *Combust Sci Technol*. 1985;42(3-4):185-205. doi:10.1080/00102208508960376
39. Rauwoens P, Vierendeels J, Dick E, Merci B. A conservative discrete compatibility-constraint low-Mach pressure-correction algorithm for time-accurate simulations of variable density flows. *J Comput Phys*. 2009;228(13):4714-4744. doi:10.1016/j.jcp.2009.03.036

40. Klein R. Numerical modelling of high speed and low speed combustion. In: Berestycki H, Pomeau Y, eds. *Nonlinear PDE's in Condensed Matter and Reactive Flows*. Springer; 2002:189-226.
41. Braack M., Becker R., Rannacher R., Warnatz J. An adaptive finite element method for combustion problems. Proceedings of the 3rd Summer Conference, Numerical Modelling in Continuum Mechanics, Charles University; 1997.
42. Kummer F. Extended discontinuous Galerkin methods for two-phase flows: the spatial discretization. *Int J Numer Methods Eng*. 2017;109(2):259-289. doi:10.1002/nme.5288
43. Kikker A, Kummer F, Oberlack M. A fully coupled high-order discontinuous Galerkin solver for viscoelastic fluid flow. *Int J Numer Methods Fluids*. 2021;93(6):1736-1758.
44. Babuška I. The finite element method with lagrangian multipliers. *Numer Math*. 1973;20(3):179-192. doi:10.1007/BF01436561
45. Pietro DAD, Ern A. *Mathematical Aspects of Discontinuous Galerkin Methods*. Mathématiques et Applications. Springer-Verlag; 2012.
46. Girault V, Rivière B, Wheeler MF. A discontinuous Galerkin method with nonoverlapping domain decomposition for the Stokes and Navier-Stokes problems. *Math Comp*. 2004;74(249):53-85. doi:10.1090/S0025-5718-04-01652-7
47. Shahbazi K. An explicit expression for the penalty parameter of the interior penalty method. *J Comput Phys*. 2005;205(2):401-407. doi:10.1016/j.jcp.2004.11.017
48. Hillewaert K. *Development of the Discontinuous Galerkin Method for High-Resolution, Large Scale CFD and Acoustics in Industrial Geometries*. Presses univ. de Louvain; 2013.
49. Krause D, Kummer F. An incompressible immersed boundary solver for moving body flows using a cut cell discontinuous Galerkin method. *Comput Fluids*. 2017;153:118-129.
50. Geisenhofer M, Kummer F, Müller B. A discontinuous Galerkin immersed boundary solver for compressible flows: adaptive local time stepping for artificial viscosity-based shock-capturing on cut cells. *Int J Numer Methods Fluids*. 2019;91(9):448-472. doi:10.1002/flid.4761
51. Kummer F, Weber J, Smuda M. BoSSS: a package for multi-grid extended discontinuous Galerkin methods. *Comput Math Appl*. 2021;81:237-257. doi:10.1016/j.camwa.2020.05.001
52. Schenk O, Gärtner K, Fichtner W. Efficient sparse LU factorization with left-right looking strategy on shared memory multiprocessors. *BIT Numer Math*. 2000;40(1):158-176. doi:10.1023/A:1022326604210
53. Schenk O, Gärtner K. Two-level dynamic scheduling in PARDISO: improved scalability on shared memory multiprocessing systems. *Parallel Comput*. 2002;28(2):187-197. doi:10.1016/S0167-8191(01)00135-1
54. Schenk O, Gärtner K. Solving unsymmetric sparse systems of linear equations with PARDISO. *Future Gener Comput Syst*. 2004;20(3):475-487. doi:10.1016/j.future.2003.07.011
55. Dennis JE, Schnabel RB. *Numerical Methods for Unconstrained Optimization and Nonlinear Equations*. Society for Industrial and Applied Mathematics; 1996.
56. Paillere H, Viozat C, Kumbaro A, Toumi I. Comparison of low-Mach number models for natural convection problems. *Heat Mass Transfer*. 2000;36(6):567-573. doi:10.1007/s002310000116
57. Vierendeels J, Merci B, Dick E. Benchmark solutions for the natural convective heat transfer problem in a square cavity with large horizontal temperature differences. *Int J Numer Methods Heat Fluid Flow*. 2003;13(8):1057-1078. doi:10.1108/09615530310501957
58. Tyliczszak A. Projection method for high-order compact schemes for low-Mach number flows in enclosures. *Int J Numer Meth HFF*. 2014;24(5):1141-1174. doi:10.1108/HFF-07-2012-0167
59. Pandya TP, Weinberg FJ. The structure of flat, counter-flow diffusion flames. *Proc Royal Soc Lond Ser A Math Phys Sci*. 1964;279(1379):544-561.
60. Spalding DB. Theory of mixing and chemical reaction in the opposed-jet diffusion flame; 1961. 10.2514/8.5626
61. Sung CJ, Liu JB, Law CK. Structural response of counterflow diffusion flames to strain rate variations. *Combust Flame*. 1995;102(4):481-492. doi:10.1016/0010-2180(95)00041-4
62. Smooke MD, Giovangigli V. Premixed and nonpremixed test problem results. In: Smooke MD, ed. *Reduced Kinetic Mechanisms and Asymptotic Approximations for Methane-Air Flames*. Springer-Verlag; 1991:29-47.
63. Matalon M, Metzener P. The effect of thermal expansion on diffusion flame instabilities. *J Fluid Mech*. 2010;647:453-472. doi:10.1017/S0022112009993016
64. Rameau JF, Schmidt-Lainé Cl. Numerical Bifurcation in Chambered Diffusion Flames. Lecture Notes in Physics; 1985:335-349; Springer, Berlin, Heidelberg.
65. Gutierrez JJ, Kummer F. A fully coupled high order discontinuous Galerkin method for diffusion flames in a low-Mach framework. TUdataLib, Data for publication; 2021. doi: 10.48328/tudatalib-412.

How to cite this article: Gutiérrez-Jorquera J, Kummer F. A fully coupled high-order discontinuous Galerkin method for diffusion flames in a low-Mach number framework. *Int J Numer Meth Fluids*. 2022;94(4):316-345. doi: 10.1002/flid.5056